

An experimental study of multiple zonal jet formation in rotating, thermally driven convective flows on a topographic beta-plane

P. L. Read, T. N. L. Jacoby, P. H. T. Rogberg, R. D. Wordsworth, Y. H. Yamazaki, K. Miki-Yamazaki, R. M. B. Young, J. Sommeria, H. Didelle, and S. Viboud

Citation: *Physics of Fluids* **27**, 085111 (2015); doi: 10.1063/1.4928697

View online: <http://dx.doi.org/10.1063/1.4928697>

View Table of Contents: <http://scitation.aip.org/content/aip/journal/pof2/27/8?ver=pdfcov>

Published by the [AIP Publishing](#)

Articles you may be interested in

[Rossby wave radiation by an eddy on a beta-plane: Experiments with laboratory altimetry](#)
Phys. Fluids **27**, 076604 (2015); 10.1063/1.4926979

[Barotropic, baroclinic, and inertial instabilities of the easterly Gaussian jet on the equatorial \$\beta\$ -plane in rotating shallow water model](#)
Phys. Fluids **26**, 056605 (2014); 10.1063/1.4875030

[Beta-plane turbulence: Experiments with altimetry](#)
Phys. Fluids **26**, 026602 (2014); 10.1063/1.4864339

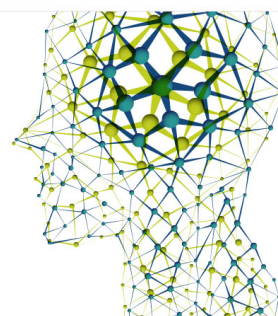
[Angular distribution of energy spectrum in two-dimensional \$\beta\$ -plane turbulence in the long-wave limit](#)
Phys. Fluids **25**, 076602 (2013); 10.1063/1.4813808

[Scaling, spectra and zonal jets in beta-plane turbulence](#)
Phys. Fluids **16**, 2592 (2004); 10.1063/1.1752928

Did your publisher get
18 MILLION DOWNLOADS in 2014?
AIP Publishing did.



THERE'S POWER IN NUMBERS. Reach the world with AIP Publishing.



An experimental study of multiple zonal jet formation in rotating, thermally driven convective flows on a topographic beta-plane

P. L. Read,^{1,a)} T. N. L. Jacoby,¹ P. H. T. Rogberg,^{1,b)} R. D. Wordsworth,^{1,c)} Y. H. Yamazaki,^{1,d)} K. Miki-Yamazaki,^{1,e)} R. M. B. Young,¹ J. Sommeria,² H. Didelle,² and S. Viboud²

¹*Atmospheric, Oceanic and Planetary Physics, University of Oxford, United Kingdom*

²*LEGI (G_INP-UJF-CNRS), Université Joseph Fourier, Grenoble, France*

(Received 15 April 2015; accepted 19 July 2015; published online 24 August 2015)

A series of rotating, thermal convection experiments were carried out on the Coriolis platform in Grenoble, France, to investigate the formation and energetics of systems of zonal jets through nonlinear eddy/wave-zonal flow interactions on a topographic β -plane. The latter was produced by a combination of a rigid, conically sloping bottom and the rotational deformation of the free upper surface. Convection was driven by a system of electrical heaters laid under the (thermally conducting) sloping bottom and led to the production of intense, convective vortices. These were observed to grow in size as each experiment proceeded and led to the development of weak but clear azimuthal jet-like flows, with a radial scale that varied according to the rotation speed of the platform. Detailed analyses reveal that the kinetic energy-weighted radial wavenumber of the zonal jets, k_{Jy} , scales quite closely either with the Rhines wavenumber as $k_{Jy} \simeq 2(\beta_T/2u_{rms})^{1/2}$, where u_{rms} is the rms total or eddy velocity and β_T is the vorticity gradient produced by the sloping topography, or the anisotropy wavenumber as $k_{Jy} \simeq 1.25(\beta_T^3/\epsilon)^{1/5}$, where ϵ is the upscale turbulent energy transfer rate. Jets are primarily produced by the direct quasi-linear action of horizontal Reynolds stresses produced by trains of topographic Rossby waves. The nonlinear production rate of zonal kinetic energy is found to be strongly unsteady, however, with fluctuations of order 10-100 times the amplitude of the mean production rate for all cases considered. The time scale of such fluctuations is found to scale consistently with either an inertial time scale, $\tau_p \sim 1./\sqrt{u_{rms}\beta_T}$, or the Ekman spin-down time scale. Kinetic energy spectra show some evidence for a $k^{-5/3}$ inertial subrange in the isotropic component, suggestive of a classical Kolmogorov-Batchelor-Kraichnan upscale energy cascade and a steeper spectrum in the zonal mean flow, though not as steep as k^{-5} , as anticipated for fully zonostrophic flow. This is consistent with a classification of all of these flows as marginally zonostrophic, as expected for values of the zonostrophy parameter $R_\beta \simeq 1.6$ – 1.7 , though a number of properties related to flow anisotropy were found to vary significantly and systematically within this range. © 2015 AIP Publishing LLC. [<http://dx.doi.org/10.1063/1.4928697>]

I. INTRODUCTION

Zonal jets, which are meant by strong flows in a predominantly east-west direction (perpendicular to the axis of rotation), are ubiquitous phenomena in planetary atmospheres. These include the

a) p.read1@physics.ox.ac.uk

b) Now at Physical Geography and Quaternary Geology, University of Stockholm, Sweden.

c) Now at School of Engineering and Applied Sciences, Harvard University, USA.

d) Now at School of Geography, Politics and Sociology, University of Newcastle upon Tyne, United Kingdom.

e) Now at School of GeoSciences, University of Edinburgh, United Kingdom.

atmosphere of the Earth itself, which exhibits at least one zonal jet in each hemisphere that varies on seasonal and shorter time scales through the combined action of large-scale differential heating and synoptic eddies.^{1,2} The nonlinear interaction of such eddies with the zonal jet stream, in particular, is a key factor in determining the structure and predictability of the atmosphere on time scales of weeks to decades.

Zonal jets play a particularly significant role in the observable atmospheres of the gas giant planets, Jupiter and Saturn, where they occur as a set of multiple streams that are closely aligned parallel to lines of latitude, alternating in direction several times between equator and pole.^{3,4} They are associated with the organization of widespread clouds of ammonia and water ice into alternating light and dark bands that dominate the visible appearance of both planets. Such dominant zonal organization of the clouds on these planets reflects the remarkable concentration of kinetic energy into the zonal jets, which appear to contain more than 90% of the total kinetic energy at the cloud tops on Jupiter.⁵ The origin of these cloud bands and associated jets is not well understood in detail, but is widely believed^{3,4} to involve the nonlinear self-organization of wave-like eddies, which interact strongly to drive and maintain them. But a remarkable feature of the zonal bands and jets on Jupiter and Saturn is their apparent robustness and stability, such that the pattern of zonal jets appears to vary little over time scales of decades or longer.⁶

The tendency for wave-like eddies to self-organize and drive and maintain zonal jet-like circulations has also been noted recently in the Earth's global oceans, in both high resolution numerical models⁷⁻¹⁰ and even in satellite observations.¹¹⁻¹³ The resulting zonal "jets" are much less prominent in ocean currents than on the gas giant planets, requiring some significant averaging in time to render them visible against the field of energetic ocean eddies. This has led to some controversy over whether such zonal flows really exist independently of the eddies that might be maintaining them or are simply artifacts of the averaging procedures.¹⁴ Such features do seem to be reproduced fairly robustly in high resolution, "eddy-permitting" numerical ocean model simulations,⁷⁻¹⁰ however, and recent observational studies appear to conclude¹¹⁻¹³ that such jet-like zonal flows are physical features of the circulation in the open ocean. The formation of multiple, parallel zonal currents is much less controversial in the context of the Antarctic Circumpolar Current,¹⁵ a broadly zonal current encircling Antarctica approximately following lines of latitude between around 40° and 60° S and largely driven by zonal winds in the atmosphere. This broad current is clearly shown to breakup into several parallel streams in a number of places, which may reflect the effects of interactions with baroclinic and barotropic ocean eddies and also with the underlying bottom topography. Bottom topography appears to play an even more significant role in promoting "zonation" of ocean currents on ocean mesoscales, sometimes resulting in the breakup of along-shore currents associated with shelving coastal bathymetry into two or more parallel streams.¹⁶

The possible role of highly dispersive and anisotropic eddies and instabilities in promoting zonally oriented mean flows has also been extensively discussed in the context of magnetized plasmas, where possible analogues of the mechanisms suggested to account for "zonation" in planetary atmospheres have been noted.¹⁷ Such zonal flows in plasmas are thought to be of major practical significance in the design of containment devices, since their presence may act as a partial barrier to radial mixing.

A variety of models, both theoretical and numerical, have been advanced (e.g., see Refs. 10 and 17-36) in attempts to account for the formation of these zonal jet-like features in various contexts. Many of these models effectively invoke the tendency of large-scale Rossby-like waves to propagate dispersively and highly anisotropically across a rotating sphere or tangent β -plane, such that energy exchanges between different scales of motion become focused into zonally elongated structures that eventually evolve into zonal jets. But many aspects of these processes remain unclear. In particular, it remains uncertain as to the respective roles of spectrally local and non-local energy exchanges in channeling kinetic energy into zonal jet-like modes. "Classical" theories of 2D or quasi-geostrophic turbulence³⁷⁻⁴⁰ have tended to emphasize the importance of spectrally local "turbulent" interactions in promoting a general upscale transfer of energy in association with a down-scale cascade of squared vorticity (enstrophy). But more recent work has suggested that non-local exchanges may play a more important role in forming jet-like flows in the presence of large-scale potential vorticity

gradients, even demonstrating the spontaneous formation of eddy-driven zonal jets in models where direct (local) eddy-eddy nonlinear interactions are artificially suppressed.^{30,31,33}

But the necessarily approximated and idealized nature of such models still leaves a number of (especially quantitative) issues uncertain.

- (i) What factors actually determine the equilibrated scale and separation of zonal jets in a forced and dissipative flow?
- (ii) What role is played by friction and dissipation in this context and is the scale of the jet and its time evolution sensitive to the physics of the dissipation (e.g., scale-selective or uniform?)?
- (iii) What determines the strength of the interaction between eddies and the zonal flow, and how is this related (if at all) to the spectrally local upscale energy cascade rate?
- (iv) Are such interactions strongly variable in time or largely statistically steady? If not, what determines the time scale of variability?
- (v) What determines the shape and nature of the resulting energy spectra in space and time?
- (vi) Are such anisotropic spectra observed in practice in realistic flows? In particular, is the k^{-5} zonal spectrum universal?^{20,21,24} and if so, under what conditions?
- (vii) What is the impact of stratification (in particular of finite Rossby deformation radius) on jet-formation mechanisms?

With regard to question (v) for weakly dissipative systems forced at small scales, for example, simplified barotropic models^{23,26,29,32,34} suggest the formation of distinct inertial ranges in the kinetic energy spectrum that make a distinction between a “classical” quasi-isotropic $k^{-5/3}$ Kolmogorov-Batchelor-Kraichnan (KBK) form for non-zonal modes and a much steeper k^{-5} spectrum for the zonal jet flow itself. Concerning the role of stratification effects, recent studies using simple shallow-water models^{41,42} suggest, for example, that a small enough (external) deformation radius could suppress the dispersive character of Rossby-like waves necessary to promote zonal jet formation, but what role (if any) is played by internal stratification?

Although numerical models of anisotropic turbulent processes can provide much insight into these questions, laboratory experiments also have an important role to play, not only in testing some of the theoretical concepts and predictions of simple models but also in allowing the exploration of other (possibly competing) processes that might contribute to either promoting or suppressing the formation of zonal jets. The task of designing an experiment to capture the essential eddy-driven processes in a form that might result in the formation of well-defined zonal jets is far from trivial, however, especially, if the intention is also to capture and investigate the formation of identifiable inertial ranges characteristic of some of the paradigms explored in idealized models. Key factors that would seem to be necessary to emulate the conditions found necessary for strong eddy-driven jet formation in simple barotropic models include (i) energetic forcing of eddies on a scale small compared with the experimental domain (and weak, or preferably no, direct forcing on large scales), (ii) strong rotation so at least large-scale motion is geostrophic, (iii) a strong beta-effect, most readily produced using conically sloping topography, such that the so-called Rhines scale $L_R \sim (u_{rms}/\beta)^{1/2} \ll L$ (where u_{rms} is a typical root mean square eddy velocity and L is the lateral scale of the experimental domain), and (iv) relatively weak viscous dissipation, requiring both large Reynolds number, based on the jet scale, and small Ekman number. A more detailed set of criteria was proposed by Galperin *et al.*²⁶ in the context of the so-called “zonostrophic” flow regime, which was identified as the extreme jet-dominated regime that typifies that found on the gas giant planets.⁵ These criteria turn out to be extremely challenging to reproduce in a normal (viscous) fluid on a feasible laboratory scale, and to our knowledge, a fully zonostrophic flow has yet to be obtained under laboratory conditions (see further discussion in Section VII).

Although a number of early experiments explored configurations that allowed the development of rectified zonal jets from forced eddies in barotropic,^{22,43–46} convective,^{47,48} and baroclinic^{47,49–51} flows, they suffered from various design flaws, e.g., that did not allow a clean separation of forcing and jet scales or were too strongly damped either by internal viscosity or bottom friction. Many of these studies (though not all) were also not well enough equipped to measure the critical diagnostics of the flows (Reynolds stresses, energy spectra, etc.) needed to fully elucidate and quantify the mechanisms that channel energy into the zonal jets. More recently, however, there have been a few

experimental studies^{52–60} that have focused more directly on creating conditions conducive to the generation of multiple parallel zonal jet flows and diagnosing them in more detail. Two of these experiments^{56–59} utilized electromechanical forcing with a fine-scale lattice of permanent magnets, following Paret and Tabeling,⁶¹ in shallow, homogeneous rotating fluid layers, though differed in their method of measurement. This method of forcing allows the spatial form and intensity of the energy injection to be well defined and controlled, although the use of fixed arrays of magnets ties the forcing to specific locations within the apparatus, which is rather different to what typically occurs in geophysical situations. Smith *et al.*⁶⁰ carried out experiments in a relatively large rotating annulus system with differential heating at the inner and outer sidewalls, while the Grenoble group^{52,55} and Read *et al.*^{53,54} utilized natural convective forcing, in the latter case by spraying dense, salty water onto the free surface of a large, cylindrical rotating tank. These approaches resulted in a more “geophysical” mode of forcing (in the latter experiments mostly on small scales), the spatial location of which was not fixed relative to the tank itself. Moreover, by running in relatively large domains (a ~ 1 m diameter rotating annulus⁶⁰ or the 13 m diameter Coriolis platform facility in Grenoble, France^{53,54}), viscous dissipation could be kept relatively low while also favoring the formation of multiple zonal jets in the presence of a topographic gradient.

In the study by Smith *et al.*,⁶⁰ a baroclinic basic zonal flow was maintained by differential heating and jets were obtained as the result of interactions with baroclinically unstable eddies in the stably stratified fluid, though it was not clear whether the multiple jets were primarily barotropic or baroclinic in character. In the earlier Coriolis and other convective experiments, in contrast, the forcing induced a basic flow that mainly consisted of statically unstable convection driving predominantly barotropic jets. A significant disadvantage of the latter study^{53,54} was that the salt water convective forcing could only be maintained for a limited period of time, so the extent to which the flows were fully equilibrated was not entirely clear. It also only proved possible to make a binary comparison in that study between jet formation with and without a topographic slope, whereas the other three experiments were able to explore the scaling of multiple jets with parameters such as rotation rate and forcing strength. At least three of these studies were able to reproduce the formation of multiple, quasi-barotropic zonal jets through the action of horizontal Reynolds stresses, though evidence for the clear inertial ranges anticipated for zonostrophic flow regimes was somewhat marginal. This was not unduly surprising, given that the conditions for achieving the zonostrophic regime were only marginally satisfied in all three cases. As we discuss below in Section VII, the conditions required to enter a fully zonostrophic regime turn out to be very demanding under normal laboratory conditions, and this set of experiments (and those presented herein) probably represents the best that can be done at the present time.

In the new experiments described here, convective forcing was employed in a similar vein to our earlier experiments,^{53,54} again using the large-scale Coriolis platform facility in Grenoble. But in the new experiments, small-scale convection was maintained by electrical heating at the bottom of the tank, which allowed the forcing to be sustained for much longer intervals than was possible using salt water forcing. Although the time scales necessary for equilibrating flows on such a large scale are quite long, it proved possible to make a number of runs whilst varying the background rotation rate over a wide range. This enabled us to explore the scaling of jet and eddy scales with factors such as rotation rate Ω and β fairly thoroughly, although it was still only possible to access marginally zonostrophic conditions. But with the long duration of these experiments, we were able to collect large quantities of data with many hundreds of realizations of horizontal velocity fields, the analysis of which is presented herein. Section II presents a detailed description of the experimental setup and measurement techniques, and the basic flow structures obtained are described in Section III. Aspects of the zonal jets obtained in the experiments are presented in Section IV and the measurements of Reynolds stresses driving them are discussed in Section V. We examine the forms of the 2D and 1D kinetic energy spectra in Section VI and concluding discussion is given in Section VII.

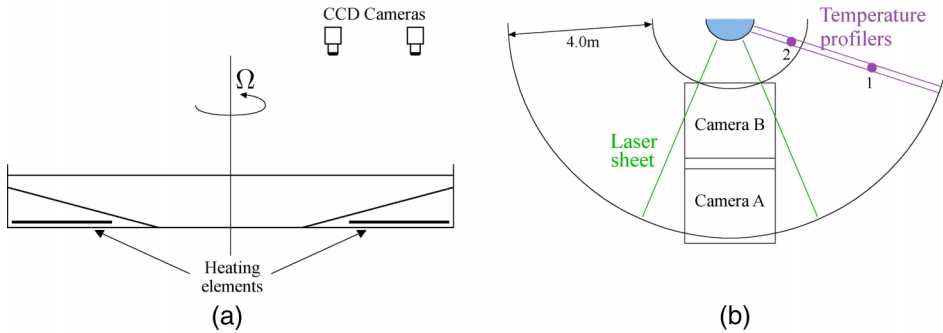


FIG. 1. (a) Schematic cross section of the Coriolis tank, indicating the sloping bottom and location of the under-floor heating wires and overhead cameras. (b) Schematic plan view of the Coriolis tank, showing the locations of the two thermal probes [(1) and (2)] and fields of view of the overhead cameras.

II. EXPERIMENT DESCRIPTION

The experiments were carried out in the 13-m diameter cylindrical tank on the Coriolis platform at Laboratoire d'Écoulements Géophysiques et Industriels (LEGI) in Grenoble, France. This tank could be filled to a depth h of up to 1 m and rotated at angular speeds of up to 0.157 rad s^{-1} (rotation period $\tau_R = 40 \text{ s}$). For these experiments, a false bottom was installed that consisted of a series of flat, segmented, aluminium sheets mounted on marine plywood wedges to create a smooth base that sloped uniformly upwards with radius between radii of 2.5 m and 6.5 m at an angle of 5.7° (0.1 rad) (see Figures 1 and 2). Together with the effect of the parabolic centrifugal

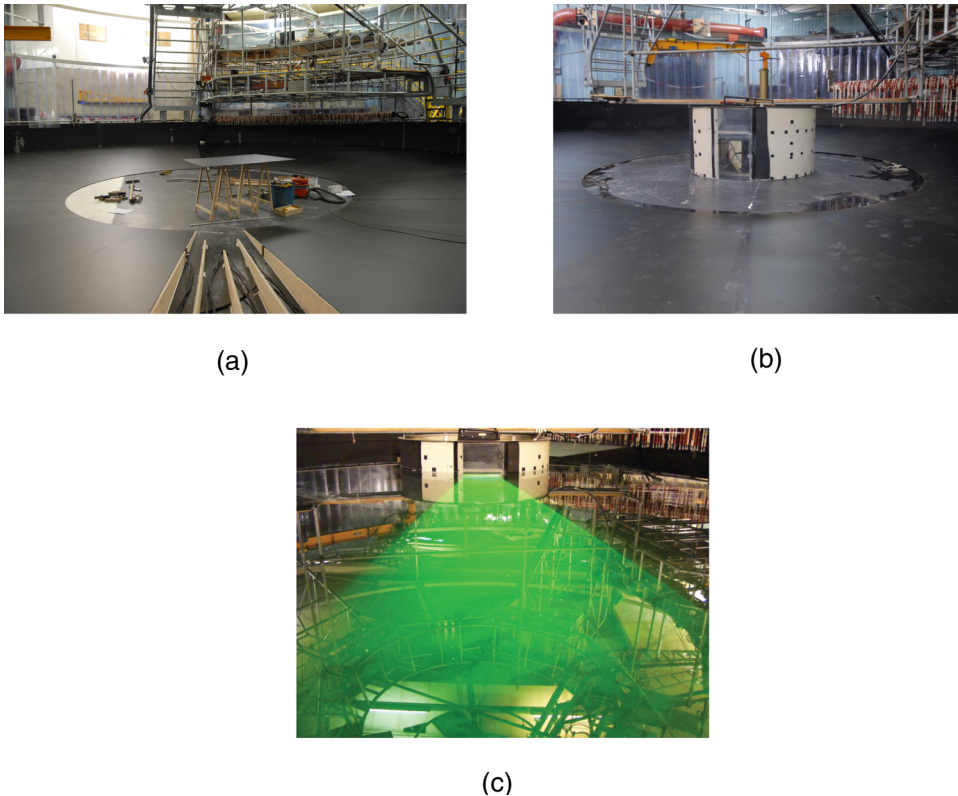


FIG. 2. Photographs of the Coriolis tank (a) during construction of the sloping bottom, illustrating the plywood support wedges and layout of heating cables underneath the aluminium segmented plates, (b) showing the central cylinder housing the illumination system and (c) the system filled with water and illuminated by the laser sheet.

deformation of the top surface due to the background rotation, this leads to a “topographic β -effect” or “planetary” vorticity gradient of the form

$$\beta_T = \frac{2\Omega}{\bar{h}} \frac{dh(r)}{dr}, \quad (1)$$

where \bar{h} is the mean value of fluid depth h at rotation speed Ω .

The tank was arranged in an annular configuration, with a central cylinder (of radius 1 m) containing optics to generate a fan-shaped, horizontal light sheet by sideways scanning of the beam from a 6 W green argon-ion laser. Most experiments used a fixed light sheet located at approximately 20–30 cm below the top surface of the fluid, though a few experiments were carried out during which the light sheet was sequentially moved to a series of depths spanning the full depth of the tank. The illuminated region could then be viewed from above by two Dalsa 1M60P CCD cameras (each with a resolution of 1024×1024 px) aligned along a radius at a height of approximately 4 m, with overlapping fields of view of $2.5 \text{ m} \times 2.5 \text{ m}$ across the tank (see Fig. 1(b)). This allowed only around 9% of the surface area of the annular region to be viewed at any one time, but this was limited by the resolution of the available cameras and the height of the roof of the building, restricting the height to which the cameras could be mounted.

The tank was typically filled with salt water of mean density $\rho = 1026 \text{ kg m}^{-3}$ at 20°C , as required to suspend a dispersion of neutrally buoyant, white tracer particles of mean diameter 0.3 mm that could be illuminated by the laser sheet. The whole tank and superstructure (to a height of around 4–6 m above the surface of the tank) was contained within a clear, plastic enclosure to reduce the effects of air currents and wind stresses at the free surface of the tank.

A. Heating and cooling

The tank was heated from below by a network of several km of electrical cables laid under the sloping bottom (see Fig. 2) and energized by a mains-driven, low voltage transformer. Heating rates of up to 11 kW could be produced by this means, evenly distributed across the whole region of the tank above the sloping bottom. It was not feasible to provide controlled cooling for such a large experimental rig, and so, it was necessary to rely on natural cooling of the upper surface to the ventilated laboratory. Experiments were carried out during November and December so external air temperatures were relatively low. Nevertheless, the continuous application of electrical heating resulted in the mean temperature of the tank rising steadily during the course of each experiment. Runs were typically terminated when the mean temperature of the tank reached 30°C , which would take of order 4–5 days, at which point the tank was drained and refilled with cold, salty water.

B. Image processing and correlation image velocimetry (CIV)

Independent images of the illuminated tracer particles were acquired using the two cameras indicated in Fig. 1(b). These were typically acquired in short bursts, spanning an interval of 3–5 s every 20–30 s. This allowed horizontal velocity fields to be obtained from combinations of pairs of images within each burst by a two-stage CIV technique.^{62,63} This enabled velocity fields to be obtained within the field of view of each camera with a spatial resolution of $\sim 5 \text{ cm}$ and a precision of better than 0.1 mm s^{-1} for flow velocities of up to 1 cm s^{-1} .

For subsequent analysis, pairs of velocity fields (one from each camera) at each time step were combined into a single velocity field covering the outermost 4 m of radius within the combined field of view of both cameras. The fields were then reprojected onto a local Cartesian coordinate system, much as used by Read *et al.*,^{53,54} so that

$$x = r_0\theta, \quad (2)$$

$$y = r, \quad (3)$$

and r_0 is a fixed value of radius (taken to be the mean value at the centre of the heated channel at $r_0 = 4.5 \text{ m}$). The final resulting fields were held as a rectangular array, equally spaced in (x, y) and

with a typical resolution of 42×81 points in x (azimuth) and y (radius), corresponding to a separation between grid points of ~ 5 cm. Such a transformation facilitated the derivation of vorticity fields and other derived diagnostics, whilst enabling the use of a coordinate system in which the x direction was everywhere in the azimuthal direction so that zonal flows could be represented clearly and unambiguously in a direction parallel to one of the coordinate axes.

The laser sheet could be positioned at different altitudes z . The velocity data presented in the paper were obtained approximately 20 cm below the free surface ($z = h - 20$ cm). However, it was noticed that the velocity dependency in z was small for the large scale flow features of interest here. This is consistent with the condition of low Rossby number with weak density stratification and baroclinity, such that the Proudman-Taylor theorem applies to a good approximation.

C. Thermal measurements

Some measurements were made of the thermal structure of the resulting flow, though it was not feasible to make detailed measurements other than at one or two specific locations. Two vertically oriented, motor-driven thermistor probes were mounted on a gantry, placed along a radius of the tank and located such that one probe (probe 1) could sample the vertical temperature structure in the middle of the channel with the sloping bottom, while the other (probe 2) could sample the structure just inside the inner radius of the sloping bottom. The latter was therefore not over a directly heated part of the tank but over an effectively adiabatic part of the lower boundary.

The sensor was located at the bottom end of each probe, and the assembly was typically held poised above the top of the free surface until a profile measurement was required. Measurements were then taken at intermittent intervals by driving both probes downwards at a steady speed into the flow while rapidly recording temperature readings. From the time series of readings during each traverse, the temperature profile could be derived, exploiting the fact that the probes were sampled in depth at a constant velocity. Care was taken to ensure that only readings taken during the downward traverse were used, so as to ensure that the probes were sampling undisturbed fluid.

III. PARAMETERS AND BASIC FLOW PATTERNS

In this section, we examine the modes of convection that energized the large scale flow and discuss the key parameters that govern its form and magnitude. The two adjustable control parameters were the tank rotation period τ_R and the mean water depth \bar{h} . Two cases have been considered in the present investigation, the “shallow” case $\bar{h} = 0.45$ m (denoted by the suffix “s” in the experiment name) and the “deep” case (suffix “d”) with $\bar{h} = 0.8$ m. Five main experiments were carried out during this investigation, each consisting of a spin-up phase, lasting around half a day to reach solid-body rotation at the desired rotation speed, followed by an extended period of up to 3–4 days, during which the flow was run to equilibration and velocity data acquired over intervals of several hours on each day of the run. All five experiments were run with the full heating rate of 11 kW, which indirectly sets the velocity scale and the related non-dimensional numbers. The whole set of external control parameters (both dimensional and dimensionless) is listed in Table I, in which different experiments are labelled by the numerical value of the rotation period in seconds (40, 80, 160, or 320) and the mean depth to which the tank was filled (“s” or “d,” respectively).

A. Convective flows and parameters

All five experiments were run with the full heating rate of 11 kW, though varied the rotation speed Ω and mean depth \bar{h} in order to span a large range in the parameters that involve β_T . By varying both Ω and \bar{h} , the effective β_T could be changed over a factor ≥ 10 , in contrast to our earlier experiments^{53,54} which only used a single rotation speed with, and without, a sloping bottom. Rotation periods $\tau_R = 2\pi/\Omega$ ranged from 40 to 320 s, which leads to a range in Ekman and Taylor

TABLE I. External parameters for main experiments.

Experiment no.	40s	40d	80d	160d	320d
\bar{h} (m)	0.45	0.8	0.8	0.8	0.8
τ_R (s)	40	40	80	160	320
$\beta_T (\times 10^{-2} \text{ s}^{-1} \text{ m}^{-1})$	6.2	3.5	1.9	0.98	0.49
$E (\times 10^{-5})$	1.65	0.522	1.04	2.09	4.18
$\mathcal{T} (\times 10^{13})$	22.5	12.6	3.16	0.790	0.197
Pr	7.2	7.2	7.2	7.2	7.2
τ_E (s)	1108	1970	2785	3940	5572
$F_B (\times 10^{-8} \text{ m}^2 \text{ s}^{-3})$	5.84	5.84	5.84	5.84	5.84
$Ra_F (\times 10^{11})$	0.149	1.49	1.49	1.49	1.49
$Ro^* (\times 10^{-3})$	3.05	1.71	4.85	13.7	38.8
ℓ_{rot} (m)	0.12	0.17	0.28	0.47	0.79
k_E (rad m ⁻¹)	52.4	37	22.4	13.4	8.0
k_D^{ext} (rad m ⁻¹)	0.47	0.35	0.18	0.088	0.044

numbers (E and \mathcal{T}), respectively, defined as

$$E = \frac{\nu}{2\Omega\bar{h}^2}, \quad (4)$$

$$\mathcal{T} = \frac{4\Omega^2 L^5}{\nu^2 \bar{h}} \quad (5)$$

(where ν is the kinematic viscosity of the fluid and L is the width of the annular channel) of 1 and 2 orders of magnitude, respectively. The Ekman spin-down time scale,

$$\tau_E = \frac{\bar{h}}{\sqrt{\nu\Omega}}, \quad (6)$$

where ν is the kinematic viscosity of the fluid, ranged over a factor of 5 from around 20 min to ~ 1.5 h.

The electrical heating at the bottom boundary averaged to a mean power density F_H of $\sim 97 \text{ W m}^{-2}$ over the heated area of the tank. This corresponds to a buoyancy flux $F_B = g\alpha F_H/(\rho c_p)$ (where g is the acceleration due to gravity, α is the volumetric expansion coefficient and c_p is the specific heat capacity of the fluid) of $5.84 \times 10^{-8} \text{ W kg}^{-1}$. This compares quite closely to the values used in our earlier experiments^{53,54} that employed a spray of dense, salty water onto fresh water to produce buoyancy forcing from above. This corresponds to quite large values of the flux Rayleigh number Ra_F , defined as

$$Ra_F = \frac{F_B \bar{h}^4}{\nu^2 \kappa} \quad (7)$$

(where κ is the thermal diffusivity of the fluid), of $1.49\text{--}14.9 \times 10^{10}$.

Given the rotation speeds employed in the current series of experiments, this leads to a range of nearly 2 orders of magnitude in the “natural Rossby number,” Ro^* , given by^{64–66}

$$Ro^* = \left(\frac{F_B}{8\Omega^3 \bar{h}^2} \right)^{1/2}, \quad (8)$$

from $\sim 10^{-3}$ – 4×10^{-2} . For all cases, however, this parameter remains $\ll 1$ so rotation would be expected to dominate the form of convection produced. Much as in our earlier Coriolis experiments,⁵⁴ convection was expected to take the form of ensembles of vertically aligned convective vortices. This was observed, as shown, for example, in Figure 3, which illustrates visualizations of some typical convective vortices during the course of experiment 80d. Crystals of malachite green dye were sprinkled into the path of vortices that were identified from concentrations of entrained tracer

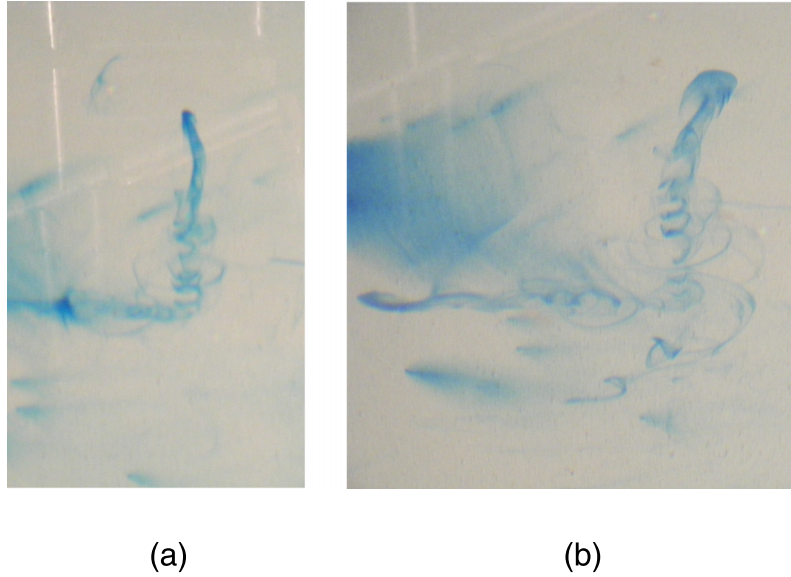


FIG. 3. Two photographs showing side views of dye visualizations of coherent convective vortices developing upwards from the heated sloping bottom of the tank (shown colored white). Vortices were visualized by dropping crystals of malachite green dye into the path of a moving vortex and observing the entrainment of dyed fluid from the boundary layer into the vortex core. This can be seen in both figures as a horizontal dye streak transitioning into a vertically oriented helical column as the dye is drawn into the convective vortex.

particles in the flow. As the dye dissolved into the water, some dyed fluid was entrained into the vortex core and advected upwards in spiral columnar trajectories, as can be seen in Fig. 3, which shows two oblique side views of some typical columnar vortices (cf. the convective columnar vortices in the experiments, e.g., of Nakagawa and Frenzen⁶⁷). The diameter of typical vortex cores was on the order of a few 10 s of cm, consistent with the rotational convective plume scale^{64,66}

$$\ell_{rot} = (3 - 5)(Ro^*)^{1/2} \bar{h}, \quad (9)$$

and included in the list of parameters in Table I. This shows fairly clearly a range of scales for convective vortices from ~ 10 to 20 cm for the highest rotation experiments to around 0.8 m for the lowest rotation rate. The corresponding typical forcing wavenumber, k_ξ , is estimated⁵⁴ as $k_\xi = \pi/\ell_{rot}$ in Table I. However, the occurrence of such convective vortices appeared to be highly intermittent, suggesting the forcing is actually not restricted to a narrow band of horizontal wavenumbers as this characterization might suggest, but it is much more broadband. This will be of some importance in interpreting kinetic energy spectra, for example.

B. Vertical stratification

Although individual convective plumes arose within convectively unstable regions of the flow, over a period of time, the general region in between such plumes gradually developed a weakly stable stratification except close to the top surface, where evaporative cooling caused the formation of an unstably stratified boundary layer. A series of temperature profiles was measured during several of the experiments using motor-driven thermistor probes, some typical results of which are presented in Figure 4. Fig. 4(a) shows a set of profiles from probe 1, located in mid-channel over the heated boundary and probe 2, located near the inner edge of the heated region over an unheated part of the lower boundary. This shows a clear difference between the conditions close to the centre of the heated channel, which exhibit a stratification that is close to being statically neutral (or sporadically weakly unstable in the lower parts of the tank), and over the unheated inner region, where the stratification is quite strongly stable (except in the evaporative cooling layer close to the top surface). This almost certainly reflects a large-scale circulation induced by the differential heating,

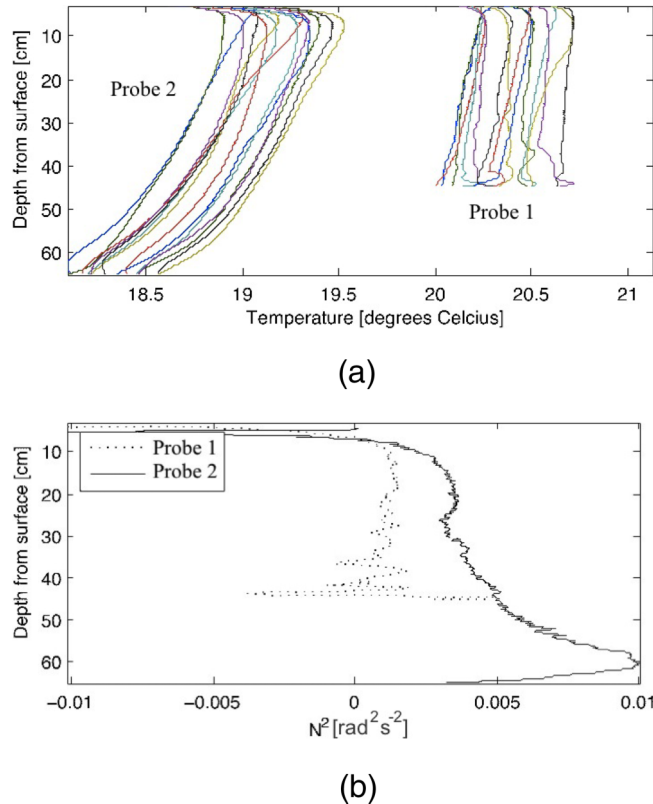


FIG. 4. (a) A set of vertical temperature profiles obtained by the two motor-driven thermal probes over an interval of 2-3 h during experiment 40d. As indicated in Figure 1(b), probe 1 is located at the central radius of the heated, sloping bottom and probe 2 is just inside the innermost radius of the sloping bottom, located over an unheated part of the tank. Profiles were obtained solely during the downward traverse of each probe. (b) An example of vertical profiles of the square of the buoyancy frequency, N^2 , derived from temperature profiles such as in (a).

leading to upwelling and near-neutral conditions over the heated channel and downwelling, stable conditions in the adiabatic region on the inner side of the heated channel. Temperatures were seen to gradually increase with time as the whole tank heated up, though this process was sufficiently slow that changes in fluid properties were relatively small and did not significantly affect, e.g., the viscosity of the fluid. The overall shape of the profiles remained largely unchanged with time, however, indicating an equilibration of the stratification structure after an initial transient phase.

Fig. 4(b) shows a couple of typical profiles of the squared buoyancy frequency, $N^2(z) = g\alpha dT(z)/dz$ (where α is the volumetric thermal expansion coefficient), corresponding to both probes. Probe 1 clearly shows regions of unstable stratification ($N^2 < 0$) at low levels, probably sampling the interior of a convective plume, and near the top surface, but with a generally stable region with $N^2 \sim 1-2 \times 10^{-3}$ rad²s⁻² at intermediate depths. The inner probe 2, in contrast, shows a quite strongly stable profile with N^2 increasing from around $3-4 \times 10^{-3}$ rad²s⁻² at mid-to upper-levels to nearly 10^{-2} rad²s⁻² near the bottom of the tank. Such a change in stratification suggests a significant transition in the mode of convection between the heated channel and the inner region.

C. Horizontal flow patterns

Following the initial spin-up of the fluid into solid-body rotation, constant bottom heating was applied and the flow was allowed to equilibrate. Much as found in the salt-driven flows in our previous Coriolis experiments,⁵⁴ the convective vortices mentioned in Subsections III A and III B were found to propagate and evolve, eventually merging and producing an equilibrated flow that

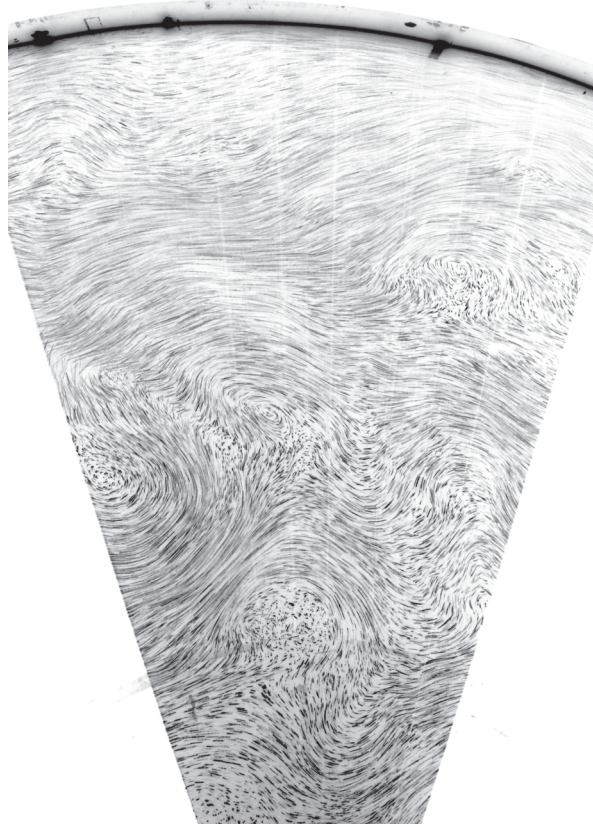


FIG. 5. Streak visualization (with inverted intensity scale) of the horizontal flow, approximately 20 cm below the top surface during the equilibration of the 40d flow (with rotation period $\tau_R = 40$ s and $D = 0.8$ m; $\beta^* = 395$). Image was made using a 30 s exposure from a hand-held digital camera located approximately 4 m above the surface of the tank.

consisted of a pattern of predominantly zonal flows and wave-like meanders. A typical snapshot of such a flow (from the 40d experiment) is illustrated in Figure 5, which shows a long-exposure streak photograph of the flow approximately 20 cm below the free surface.

Flows were typically highly chaotic, but with patterns of slowly evolving and strongly meandering zonal jets interspersed with sporadic closed vortices of either signs. Typical flow speeds were on the order of a few mm s^{-1} . The characteristic length scales of both zonal flows and associated waves and eddies varied between experiments, with the largest scales being found at the lowest rotation rates and the smallest scales at the highest rotation speeds.

The non-axisymmetric meanders in the zonal jet-like flows were seen to propagate preferentially in the prograde direction, much as would be expected for barotropic Rossby waves with the sense of β implied by the imposed topography. Figure 6 shows an example of a Hovmöller (azimuth-time) map of radial velocity perturbations along a line of constant radius within the 40d experiment. This clearly shows features that are oscillatory in azimuth with ~ 2 wavelengths within the observational window, propagating in the $+\theta$ direction at a reasonably uniform rate. Some variations are evident, however, such as merging or splitting events, indicating chaotic behavior. The observed drift periods of the waves are between around 500 and 1500 s, consistent with their space-time spectra (not shown). These are broadly consistent with the phase speeds of linear Rossby waves, for which

$$\omega \simeq \frac{+\beta_T k_x}{(k_x^2 + k_y^2 + k_D^2)}, \quad (10)$$

where k_x and k_y are the azimuthal and lateral wave numbers, respectively, assuming that $k_x \sim k_y$, and k_D is a Rossby deformation wavenumber. This appears to be generally the case for all the

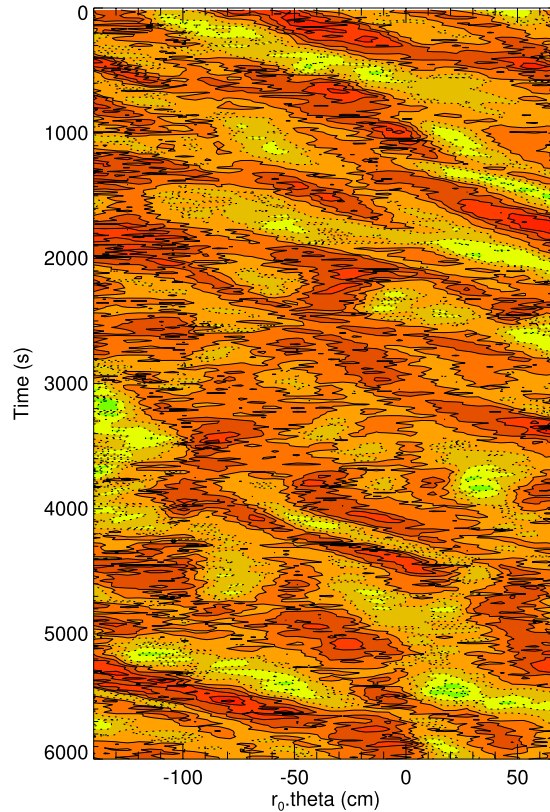


FIG. 6. A typical azimuth-time map of radial velocity perturbations at a depth of 20 cm below the top surface during a 2 h period at mid-radius during the 40d experiment (with rotation period $\tau_R = 40$ s and $D = 0.8$ m; $\beta^* = 395$).

experiments discussed here with waves propagating “eastward” dispersively (see the supplementary material⁶⁸ for other examples). It is also consistent with k_D being relatively small compared with k_x and k_y .^{41,42} This is evidently the case if k_D is taken to be the inverse external (barotropic) deformation radius, $k_D^{ext} = 2\pi\Omega/\sqrt{g\bar{h}} = 1/L_d^{ext}$ (see Eq. (18) and Table I below), since L_d^{ext} is actually larger than the size of the domain for all of the present experiments (see Table I). This implies that barotropic shallow water Rossby waves spanning the entire depth of the tank are quasi-nondivergent and are fully dispersive and anisotropic (see Section IV A).

IV. ZONAL JETS

One of the most striking aspects of the horizontal flow patterns that were seen to emerge in these experiments was the spontaneous development of meandering, mostly azimuthal (zonal) jets linking chaotic patterns of discrete vortices. These jets were typically of a strength comparable with those of the non-axisymmetric eddies, though the intensity varied systematically with radius with the stronger jet flows occurring at smaller radii. The number and radial scale of the jets varied significantly between experiments, with the largest number of relatively narrow jets occurring at the highest values of Ω , but with just one or two prograde jets apparent at the lowest value of Ω .

Figure 7 illustrates some examples of the radial and temporal variability of the zonal flows in each of the five experiments conducted. It shows radius-time, colour-shaded maps of the zonal mean zonal velocity within the observation window for a 2 h period for each experiment, ranging from $\tau_R = 320$ s (a) to 40 s [(d) and (e)]. From this, it is clearly apparent that the zonal flows, though predominantly prograde, change sign several times with radius with a radial scale that get uniformly smaller in going from (a) to (e). In every case, however, the “jets” evidently meander

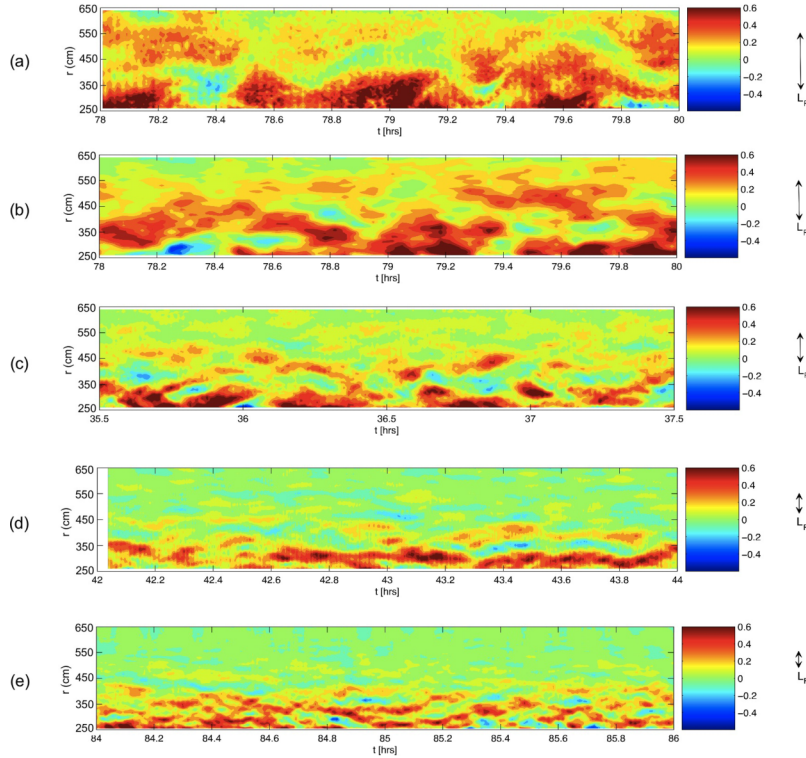


FIG. 7. Time series of the radial structure of the azimuthal flow velocity, averaged in azimuth across the combined field of view of cameras A and B (see Fig. 1(b)), for various values of rotation period and water depth. Parameters correspond to (a) $\tau_R = 320$ s, $D = 0.8$ m ($\beta^* = 43$), (b) $\tau_R = 160$ s, $D = 0.8$ m ($\beta^* = 91$), (c) $\tau_R = 80$ s, $D = 0.8$ m ($\beta^* = 180$), (d) $\tau_R = 40$ s, $D = 0.8$ m ($\beta^* = 395$), and (e) $\tau_R = 40$ s, $D = 0.45$ m ($\beta^* = 581$). Colour bars indicate the azimuthal flow velocity in cm s^{-1} .

significantly on time scales of 10–40 min, undergoing merging or splitting events so that no single jet persists unaltered throughout the observation period (see the supplementary material⁶⁸ for other examples).

A. Length scales

This systematic variation in the lateral scale of the zonal jets is reminiscent of the trend found in our earlier experiments,⁵⁴ where it was suggested that the jet length scale roughly followed a scaling similar to that of the Rhines scale $L_R \sim (u_{rms}/\beta_T)^{1/2}$. Table II lists a number of parameters derived from various measurements of the flow properties. These include the horizontal kinetic energy (also partitioned into zonal mean and “eddy” parts, ZKE and EKE, such that $\text{TKE} = \text{ZKE} + \text{EKE}$), from which respective values of u_{rms}^T , u_{rms}^Z , and u_{rms}^E could be obtained. This indicates that although the total kinetic energy (TKE) varied by more than a factor ~ 2 between experiments 40s and 320d, the EKE remained fairly uniform at around $2\text{--}2.5 \text{ mm}^2 \text{ s}^{-2}$. ZKE, on the other hand, varies by a factor of almost 5 between experiments 40s and 320d, indicating a substantial shift towards a more zonally dominated flow at the lowest rotation rates.

Given this information, it is straightforward to derive estimated values for the Rhines wavenumber, k_R ,

$$k_R = \left(\frac{\beta_T}{2u_{rms}} \right)^{1/2} \quad (11)$$

and the corresponding length scale, L_R , is given by

$$L_R = \frac{\pi}{k_R}, \quad (12)$$

TABLE II. Derived parameters for main experiments.

Experiment no.	40s	40d	80d	160d	320d
TKE ($\times 10^{-6} \text{ m}^2 \text{ s}^{-2}$)	3.57	3.12	4.93	7.31	7.88
EKE ($\times 10^{-6} \text{ m}^2 \text{ s}^{-2}$)	2.52	1.75	2.49	2.54	2.92
ZKE ($\times 10^{-6} \text{ m}^2 \text{ s}^{-2}$)	1.05	1.37	2.44	4.77	4.96
u_{rms}^E ($\times 10^{-3} \text{ m s}^{-1}$)	2.25	1.87	2.23	2.27	2.42
ϵ ($\times 10^{-10} \text{ m}^{-2} \text{ s}^{-3}$)	16.8	8.05	8.85	7.92	7.08
β^*	581	395	180	91	43
k_R^E (rad m^{-1})	3.71	3.06	2.06	1.47	1.01
k_β (rad m^{-1})	5.81	4.99	3.45	2.47	1.70
k_D^{int} (rad m^{-1})	57	31.8	15.9	8.0	4.0
β_D^{*int}	0.08	0.18	0.33	0.67	1.26
β_D^{*ext} ($\times 10^3$)	1.24	1.50	2.73	5.54	10.4
$\tilde{\beta}^{int}$	0.15	0.31	0.53	0.96	1.64
$\tilde{\beta}^{ext}$	445	563	978	1760	3000
$R_\beta = k_\beta/k_R$	1.57	1.63	1.67	1.68	1.69
k_{yJ} (rad m^{-1})	8.39	7.46	5.36	3.97	3.51
$C(K_E, K_Z)$ ($\times 10^{-10} \text{ W kg}^{-1}$)	2.64	0.76	0.50	2.65	5.16
Standard error ($\times 10^{-10} \text{ W kg}^{-1}$)	0.97	0.34	0.57	0.66	0.52
$C(K_E, K_Z)/\epsilon$	0.157	0.094	0.056	0.34	0.73
τ_{conv} (s)	960	832	1089	1270	1713
τ_{ZKE} (s)	3839	937	2398	2110	1998
τ_{pT} (s)	818	1126	1387	1719	2394
τ_{drift} (s)	350	902	1540	1428	1430
Anisotropy α_I	0.127 (± 2)	0.136 (± 2)	0.239 (± 2)	0.375 (± 2)	0.412 (± 3)
ϵ_{spec} ($\times 10^{-10} \text{ m}^{-2} \text{ s}^{-3}$)	9.4	5.6	4.8	5.4	5.0

where u_{rms} is a measure of the typical horizontal velocity. This is commonly assumed to be the rms eddy horizontal velocity u_{rms}^E ,^{54,69,70} for which k_R is designated k_R^E , e.g., in Table II. Some studies have associated the Rhines scale with a rms measure of the mean zonal velocity itself \bar{u}_{rms}^Z ,^{27,55} however, the k_R for which we here designate as k_R^Z . We investigate this distinction further below.

These definitions of a Rhines length scale are frequently interpreted as representing a measure of the scale at which β -effects become significant in the vorticity conservation equation. For flows described by a $k^{-5/3}$ inverse energy cascade inertial range, however, Galperin *et al.*^{26,29} note that the “frictional wavenumber” at which energy dissipation at large scales leads to a flattening of the kinetic energy spectrum is $\sim k_R$ to within a factor of order unity, suggesting a rather different interpretation for k_R as the scale at which large-scale dissipation becomes significant, with more weakly dissipated flows favoring smaller values of k_R . These definitions of k_R lead naturally to a family of non-dimensional beta-parameters, β^* , measuring the (squared) ratio of the Rhines scale to that of the domain itself. Based on u_{rms}^E , we define β^* to be

$$\beta^* = \frac{\beta_T L^2}{2u_{rms}^E}, \quad (13)$$

where L represents the length scale of the apparatus, assumed here to be the radius of the tank so $L = 6.5$ m, which is also tabulated in Table II. β^* in the present work varies by more than an order of magnitude between experiments 40s and 320d, though even at its lowest value is much larger than unity. This indicates that potential vorticity constraints are likely to be dominated by “planetary vorticity” effects represented by β_T for all five experiments investigated here, though with substantial variations between them.

Fig. 7 also indicates estimated values for L_R^E for each experiment in the rightmost column, using Eq. (12) and $u_{rms} = u_{rms}^E$. This provides a clear indication that the radial “wavelength” of the zonal mean jets appears to follow a roughly similar trend to that of the Rhines length scale.

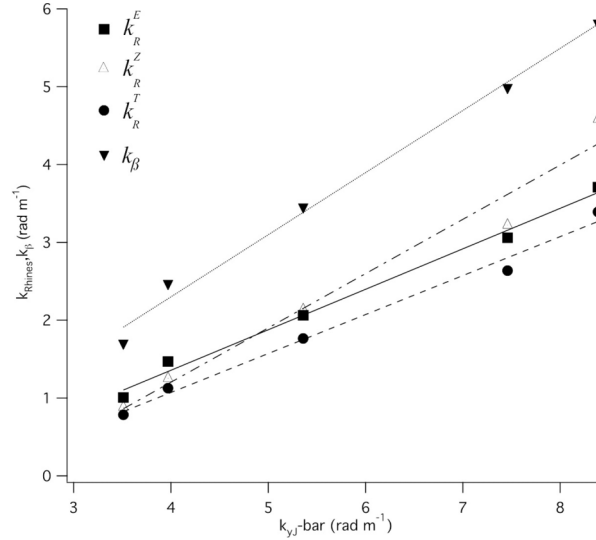


FIG. 8. Dependence of kinetic energy weighted radial wavenumber of the azimuthally and time-averaged zonal flow on Rhines wavenumber k_R and k_β . k_R was computed using either the rms eddy velocity (solid squares)– k_R^E , the rms zonal velocity (open triangles)– k_R^Z , or total rms velocity– k_R^T (solid circles) k_R was computed using the topographic β_T (see text). k_β is shown as solid inverted triangles. The solid line represents a fit to k_R^E (with gradient 0.52 ± 0.03 and intercept -0.72 ± 0.16), the dashed line a fit to k_R^T (with gradient 0.50 ± 0.03 and intercept -0.93 ± 0.18) and the dashed-dotted line a fit to k_R^Z (with gradient 0.70 ± 0.07 and intercept -1.59 ± 0.42). The fit to k_β is shown as a dotted line with gradient 0.80 ± 0.04 and intercept -0.89 ± 0.25 .

In order to test this link more quantitatively, the ZKE-weighted radial (meridional) wavenumber of the observed zonal flow was computed from the velocity data in the form

$$\overline{k_{yJ}} = \frac{\langle \overline{k_y} E_Z(\overline{k_y}) \rangle}{\langle E_Z(\overline{k_y}) \rangle}, \quad (14)$$

where $E_Z(\overline{k_y})$ is the power spectral density of zonal mean kinetic energy at radial (meridional) wavenumber $\overline{k_y}$ and angled brackets imply a time-average. Because the variation in \overline{u} oscillated with an amplitude that decreased strongly with r , the radial kinetic energy spectrum was obtained after weighting u by a factor of $(r/r_0)^3$. This led to the values of $\overline{k_{yJ}}$ listed in Table II.

Figure 8 plots the derived values of $\overline{k_{yJ}}$ against k_R , as obtained from Eq. (11) using either u_{rms}^E , u_{rms}^Z or the total rms velocity, u_{rms}^T . This clearly shows that $\overline{k_{yJ}}$ scales almost linearly with either k_R^E or k_R^T , except perhaps at the lowest value of k_R in each case, where the radial wavelength of the jets becomes comparable with L . Fitting a simple straight line to these data leads to a gradient of 0.51 ± 0.03 for both k_R^E and k_R^T cases and a y -intercept of -0.72 ± 0.16 for k_R^E or -0.93 ± 0.18 for k_R^T . Although not perfectly linear, the fit in both cases is good (correlation coefficient of 0.996), strongly indicating that the lateral wavenumber of the zonal jets scales closely with these definitions of the Rhines scale to a good approximation, except when the lateral scale approaches that of the domain itself. The actual scaling is close to $\overline{k_{yJ}} \approx 2k_R$ according to this measure, though may be closer to $\overline{k_{yJ}} \approx 2.5k_R$ if the fit is made to go through the origin. If u_{rms}^Z is used to define k_R , the plot shows a similar linear trend to the other two measures of u_{rms} with gradient of 0.7 ± 0.07 , but the linear fit is marginally less good (correlation coefficient of 0.985) and is even further from passing through the origin (y -intercept of -1.59 ± 0.42). The poorer fit is affected by the variation in the ZKE fraction of the total across this range of experiments. Although the evidence presented here does not strongly favor any one measure over the other possible alternatives, the data would seem to marginally favor using either u_{rms}^E or u_{rms}^T to define k_R or L_R , and we therefore use the scales based on u_{rms}^E in the following discussion.

The other main length scale in beta-turbulence is represented by the anisotropy wavenumber, k_β , given by^{20,21,71,72}

$$k_\beta = \left(\frac{\beta_T^3}{\epsilon} \right)^{1/5}, \quad (15)$$

where ϵ is the upscale energy transfer rate. k_β is defined^{70,72} as representing the scale at which the eddy turnover time scale, $\tau_k = \epsilon^{-1/3} k^{-2/3}$, becomes comparable with the inverse of the Rossby wave frequency, $\omega^{-1} \simeq k/\beta$, and estimates the smallest scale at which anisotropic Rossby wave propagation begins to affect the turbulent inverse cascade. ϵ is not easy to measure directly, but can be estimated^{23,34,54} as $\epsilon \simeq (u_{rms}^T)^2/(2\tau_E)$, based on the total horizontal kinetic energy. This, together with the implied k_β , is listed for each experiment in Table II and shown as inverted triangles and a dotted line in Fig. 8. k_β is seen to be consistently greater than k_R , such that $\overline{k_{yJ}} \simeq 1.25k_\beta$. This is as expected for zonostrophic or transitional flows, which are defined to be relatively weakly dissipated at large scales and consequently have a well developed inverse energy inertial range and well defined “frictional wavenumber” approximated by k_R (in contrast to frictionally dominated flows for which k_R shifts to a higher wavenumber, potentially comparable with other scales such as k_β). The linear fit to k_β in Fig. 8 seems to be as good as for any of the measures of k_R (correlation coefficient 0.996) so could be consistent with a direct scaling of $\overline{k_{yJ}}$ on k_β , although the theoretical basis for such a scaling is not clear.

The ratio,

$$R_\beta = k_\beta/k_R, \quad (16)$$

is known as the *zonostrophy index* and may be regarded as a measure of how strongly anisotropic the turbulent flow may be (see Refs. 26, 29, and 34). The values of R_β inferred from Table II of around 1.6–1.7 indicate that these flows are in the transitional regime rather than being fully zonostrophic,^{26,29} which is similar to the conditions inferred for the Earth’s oceans where eddy-driven zonal jets are thought to be relatively weak, chaotic, and “latent” (in the sense⁹ of being no stronger in kinetic energy than the eddies and therefore not very prominent). This is in contrast to the highly zonostrophic, intense and almost rectilinear jets found in the atmospheres of gas giant planets,⁵ where R_β was inferred to be around 5–6. The experimental values of R_β are also consistent with the near equality of ZKE and EKE for these experiments, although the fraction of TKE represented by ZKE clearly increases strongly and systematically with R_β from around 0.29 at $R_\beta = 1.57$ to more than 0.6 at $R_\beta = 1.7$.

Similar trends are also apparent in the variation of the flow anisotropy, α_I , which may be defined as^{8,57}

$$\alpha_I = \frac{\langle u^2 \rangle - \langle v^2 \rangle}{\langle u^2 \rangle + \langle v^2 \rangle}, \quad (17)$$

where u and v are the velocity components in the zonal (x) and radial or lateral (y) directions, respectively, and $\langle() \rangle$ represents an ensemble mean over space and time. This parameter provides a measure of the “zonality” of the flow, ranging in possible values from -1 for purely radial motion, $+1$ for purely zonal motion, and zero for perfectly isotropic flow. As indicated in Table II, α_I varies systematically with R_β in these experiments from small values ~ 0.13 at the smallest R_β to more than 0.4 at the largest R_β , indicating a clear trend towards more zonally dominated flows at larger R_β .

Various measures of the Rossby deformation radius are also important in relation to the Rossby dispersion relation and scales relating to instabilities and the generation of eddying motions. The external deformation radius, L_D^{ext} , is defined as

$$L_D^{ext} = \frac{\sqrt{g\bar{h}}}{2\Omega} \quad (18)$$

representing the ratio of the external shallow surface gravity wave speed to 2Ω . This is represented in Table II by $k_D^{ext} = \pi/L_D^{ext}$, where it is clear that k_D^{ext} is relatively small for all experiments,

corresponding to $L_D^{ext} > L$. The corresponding dimensionless parameters

$$\beta_D^{*ext} = \frac{\beta_T (L_D^{ext})^2}{u_{rms}^E} = \left(\frac{L_D^{ext}}{L_R} \right)^2 \quad \text{and} \quad (19)$$

$$\tilde{\beta}^{ext} = \beta_T \frac{(L_D^{ext})^5}{\epsilon^3} = \left(\frac{L_D^{ext}}{L_\beta} \right)^5 \quad (20)$$

are both relatively large (see Table II). β_D^{*ext} measures the squared ratio between the external deformation radius L_D^{int} and L_R , while $\tilde{\beta}^{ext}$ indicates the ratio between L_D^{ext} and L_β . As discussed above, the fact that L_D^{ext} is large compared to either scale indicates that barotropic Rossby waves are quasi-nondivergent, highly dispersive, and anisotropic^{23,41} in these experiments. The internal deformation radius is defined by

$$L_D^{int} = \frac{N\bar{h}}{2\Omega}, \quad (21)$$

where N is the mean buoyancy frequency as defined above and is represented in Table II by $k_D^{int} = \pi/L_D^{int}$. This wavenumber is generally relatively large, corresponding to a small Burger number (defined as $Bu = 1/(k_D^{int}L)^2$ and representing the squared ratio of the internal deformation radius to the domain scale), though it becomes comparable with k_R^E and k_β at the lowest rotation speeds investigated here. The corresponding dimensionless parameters

$$\beta_D^{*int} = \frac{\beta_T (L_D^{int})^2}{u_{rms}^E} = \left(\frac{L_D^{int}}{L_R} \right)^2 \quad \text{and} \quad (22)$$

$$\tilde{\beta}^{int} = \beta_T \frac{(L_D^{int})^5}{\epsilon^3} = \left(\frac{L_D^{int}}{L_\beta} \right)^5 \quad (23)$$

are both relatively small, in contrast to those based on L_D^{ext} (see Table II), indicating that internal baroclinic Rossby waves may be more divergent and consequently much less dispersive and anisotropic^{23,41} than their barotropic counterparts.

B. Time variations

Fig. 7 indicates that the zonal mean jets fluctuate erratically both in their structure and in their amplitude on time scales of several tens of minutes. These fluctuations include meandering of the jet cores in radius (though only over limited ranges in r), merging and splitting of both prograde and retrograde jets and variations in the strength of each jet.

The time variations in the strength of the jets can be seen in time series of the ZKE averaged across the observed domain. Figure 9(a) shows a typical ZKE time series, taken from experiment 80d. This shows quite strong fluctuations about a mean value of around $2.4 \mu\text{J kg}^{-1}$ by a factor of 2 or more. A dominant time scale is also evident from this time series, suggesting a noisy but reasonably clear cyclic variation. The frequency spectrum in Fig. 9(c), computed over a complete run of around 10 h, reveals a number of strong peaks centered at around 4×10^{-4} Hz and its harmonics, as well as much lower and higher frequency components. The dominant period of these fluctuations in ZKE, τ_{ZKE} , was computed over 1000 time samples for each experiment and is also listed in Table II. These values are quite variable and uncertain, but with some marginal indication of a generally decreasing trend in dominant period with increasing R_β , though the frequency spectrum is often not dominated by a single frequency peak.

The corresponding time series and spectrum for the eddy kinetic energy for experiment 80d are illustrated in Figs. 9(b) and 9(d). The EKE time series shows somewhat weaker variability than is apparent in ZKE, though with fluctuations on similar time scales. This is evident in the power spectrum in Fig. 9(d), which shows a strong peak at very low frequencies $\sim 10^{-4}$ Hz and weaker peaks corresponding to periods of 1500–2500 s, including a peak close to the eddy drift time scale τ_{drift} (see below). In general, however, the frequencies found to be dominant in EKE variations do

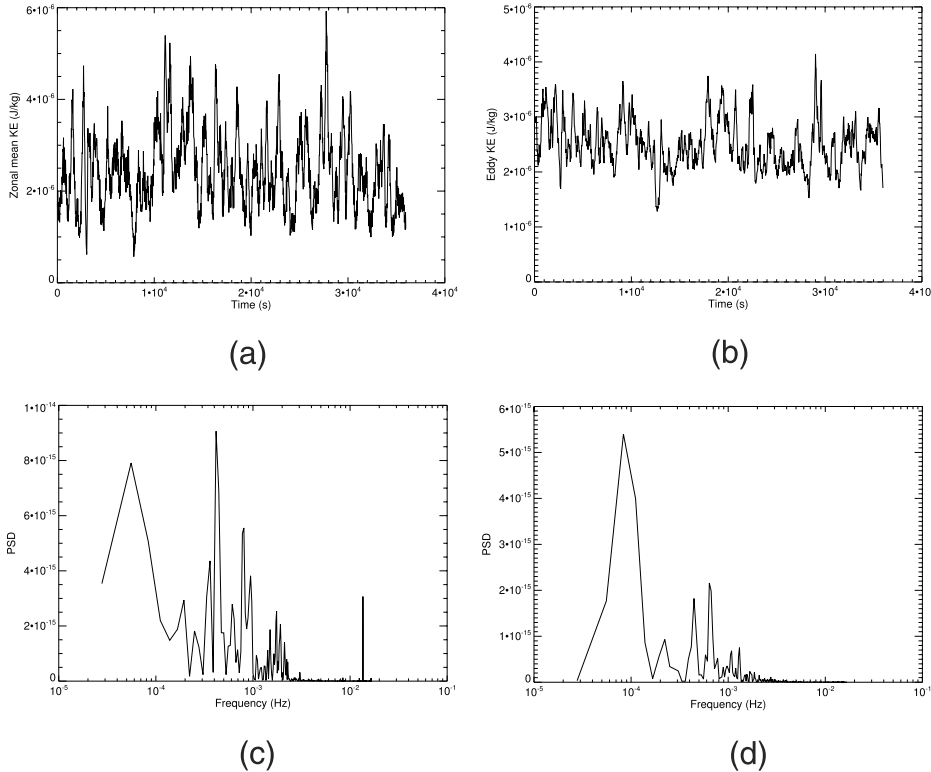


FIG. 9. (a) Time series of the kinetic energy of the azimuthally averaged flow and (b) time series of the eddy kinetic for experiment 80d ($\beta^* = 180$) over a period of 10 h following flow equilibration. (c) and (d) frequency power spectra of the time series shown, respectively, in (a) and (b).

not correlate strongly with those found for ZKE and the fluctuations in EKE and ZKE do not seem to be strongly correlated. Further aspects of these time scales will be discussed Sec. V.

V. EDDY-ZONAL FLOW INTERACTIONS

The zonal jets produced in these experiments are strongly reminiscent of those in our earlier, salt-driven convection experiments,⁵⁴ in which it was clearly shown that the jets were produced as the result of nonlinear eddy-zonal flow interactions. In this section, we explore quantitatively the possible origins of the jets in the present experiments as the result of similar, quasi-barotropic eddy-zonal flow processes.

A. Reynolds stresses and zonal accelerations

The near-barotropic character of the large-scale flows found in the present experiments suggests that the zonal jets discussed in Sec. IV are likely to have arisen from the nonlinear rectification effects of zonally propagating, Rossby wave-like eddies as they evolve and break. Quantitatively, the strength of these interactions is determined by the divergence of the horizontal Reynolds stress \mathbf{F}_R which, in cylindrical polar coordinates, can be written as

$$\nabla \cdot \mathbf{F}_R \approx \frac{1}{r} \frac{\partial}{\partial r} (r \overline{u'v'}), \quad (24)$$

where the effects of the vertical Reynolds stress, $\partial/\partial z (\overline{w'u'})$, have been neglected. If this hypothesis is valid, then time variations in zonal mean velocity \bar{u} should be significantly anti-correlated with the radial divergence of the horizontal Reynolds stress, $\overline{u'v'}$.

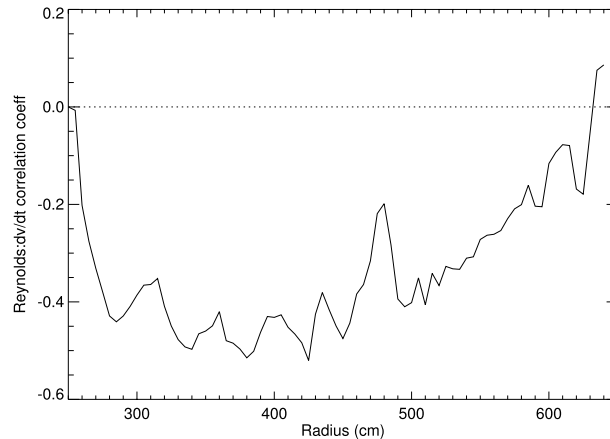


FIG. 10. Correlated relationship between horizontal Reynolds stress divergence $\nabla \cdot (\overline{u'v'})\mathbf{e}_r$ and observed acceleration of the azimuthal mean flow $\partial\bar{v}/\partial t$ in the form of a profile of the correlation coefficient as a function of radius for experiment 80d.

Given the time series of velocity field measurements in each of our experiments, both Reynolds stress and $\partial\bar{u}/\partial t$ can be computed as a function of radius and time, and the correlation coefficient between them, C , is determined over time intervals long enough to observe strong variations in ZKE. Figure 10 shows a profile of the correlation coefficient between Reynolds stress divergence and $\partial\bar{u}/\partial t$ as a function of radius, computed over the full 10 h of the run. This clearly shows a significantly coherent anti-correlation between zonal flow acceleration and Reynolds stress divergence, with values of the correlation coefficient in the range $-0.5 < C(r) < -0.3$ except close to the outer boundary of the tank, where both zonal flows and eddies are relatively weak. This indicates a statistically significant anti-correlation, and the zonal flow accelerations inferred from the values of $(1/r)\partial/\partial r(\overline{ru'v'})$ are of a similar magnitude to (though somewhat smaller than) the measured values of $\partial\bar{u}/\partial t$. In this respect, the zonal flow appears to respond quite closely to the Reynolds stresses much as found in previous experiments.^{53,54}

The fact that the measured zonal accelerations do not quite match those consistent with the observed Reynolds stress divergence, however, indicates that other processes may also be active in accelerating or modulating the mean zonal flow. These could conceivably include (a) residual wind stress effects, (b) baroclinic eddy stresses, or (c) effects related to the open boundaries of the measured domain. Wind stresses may have been associated with the possible interaction of the rotating free surface with the air immediately above the tank, although the setup was designed to enclose the body of air above the tank inside a plastic-lined enclosure to bring it into solid-body rotation with the tank itself. Wind stresses might then be expected to tend to reduce differential motion in the water relative to the tank itself, though this is hard to quantify. Baroclinic effects are most likely to have been significant near the inner radius of the domain, close to the boundary of the heated bottom plate where horizontal thermal gradients are largest and the stratification is relatively stable. The zonal flow was found to be strongest in the inner part of the tank, where eddies and jet meanders were also most prominent, so baroclinic interactions with the zonal flow may have been most significant in this region of the flow. The kinetic energy tendencies associated with the open (non-periodic) zonal boundaries of the measurement domain associated with advection of zonal and eddy kinetic energy were computed explicitly for each of the experiments in the present series and found to be no larger than a few percent of the computed $C(K_E, K_Z)$ values listed in Table II.

B. Kinetic energy conversion rates

Given the Reynolds stress and zonal velocity \bar{u} as a function of radius and time, we can compute the mean kinetic energy conversion rate as

$$C(K_E, K_Z) = - \frac{\int (\bar{u}/r) \frac{\partial}{\partial r} (\overline{ru'v'}) r \cdot dr}{\int r \cdot dr} \quad (25)$$

$$= \frac{\int (\partial \bar{u} / \partial r) (\overline{u'v'}) r \cdot dr}{\int r \cdot dr}, \quad (26)$$

where Eq. (25) is linked to Eq. (26) by an integration by parts. This leads to time mean values of $C(K_E, K_Z)$, as listed in Table II, of order $0.5\text{--}5 \times 10^{-10} \text{ W kg}^{-1}$, though with relatively large standard errors. These values are of the same order of magnitude as, though generally somewhat smaller than, the inferred values for ϵ based on the total kinetic energy. This is to be expected as the latter represents the total energy transfer towards dissipation at large scales, whereas $C(K_E, K_Z)$ only represents the fraction of that transfer that ends up directly in the mean zonal flow. The ratio $C(K_E, K_Z)/\epsilon$ does appear to show some evidence for a monotonically growing trend with increasing R_β and decreasing β^* , from around 0.1 at low values of R_β to around 0.7 at the highest values, though how significant this may be is not clear.

The large standard error on $C(K_E, K_Z)$ appears to reflect a strong variation of this conversion rate with time, with a standard deviation that is actually significantly larger than the mean value. Figure 11(a) shows an example of a time series of $C(K_E, K_Z)$, computed at each measured time step during a run of experiment 80d. This clearly shows noisy fluctuations with the instantaneous value of $C(K_E, K_Z)$ varying by factors of up to $\sim 5 \times 10^{-9} \text{ W kg}^{-1}$ and even sporadically changing sign. The corresponding histogram of such variations is shown in Fig. 11(b), which shows a peaked distribution that is almost symmetrical about zero with a HWHM of around $2 \times 10^{-9} \text{ W kg}^{-1}$. The time-mean value was consistently positive, however, and the standard error (listed in Table II) confirmed its statistical significance. This kind of behavior was seen in all five experiments.

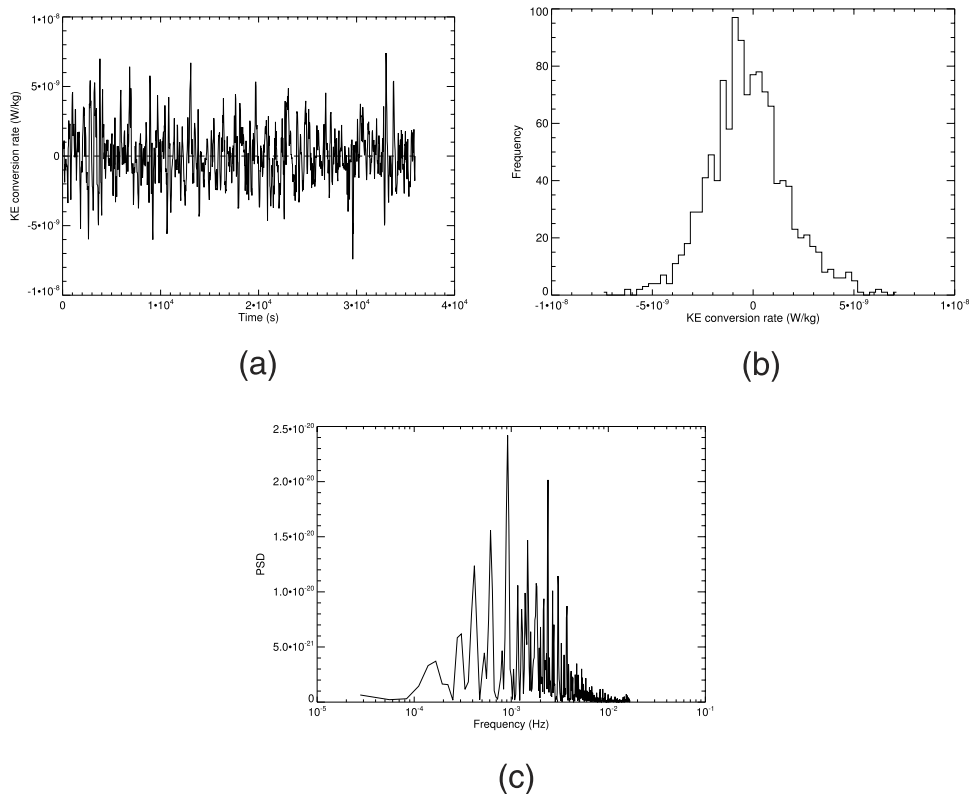


FIG. 11. (a) Time series of eddy-zonal flow kinetic energy conversion rate $C(K_E, K_Z)$, measured at 20 cm below the top surface in experiment 80d ($\beta^* = 180$) over a period of approximately 10 h; (b) histogram of measured values of $C(K_E, K_Z)$ corresponding to (a); and (c) frequency power spectrum of the time series shown in (a).

In each case, the time variation of $C(K_E, K_Z)$ was seen to exhibit a noisy, semi-periodic form with a hint of a characteristic time scale. This is further suggested, for example, in Fig. 11(c), which shows the frequency spectrum of the time series in Fig. 11(a). A peaked spectrum is clearly seen with a dominant frequency of around 9×10^{-4} Hz and a period $\tau_{conv} \simeq 1089$ s, together with some higher frequency components that may include harmonics of the dominant frequency. The dominant period, τ_{conv} , was estimated for each experiment from the corresponding frequency spectrum of $C(K_E, K_Z)(t)$ and the results are listed in Table II from which a clear trend is evident. With the exception of experiment 40s, τ_{conv} is seen to decrease almost monotonically with β^* (and increase with R_β) over the range $832 \leq \tau_{conv} \leq 1713$ s. The frequencies identified here, however, were not always dominant throughout the respective time series, so this trend in time scale should be regarded as indicative rather than conclusive.

C. Time scales for energy conversion

The large fluctuations in $C(K_E, K_Z)$ with time were somewhat unexpected, and it is of interest to consider what might be the underlying cause. It is notable that the trend in τ_{conv} does not seem to be correlated with that of ZKE fluctuations, whose time scale τ_{ZKE} generally appears to increase with β^* and decrease with R_β .

An important consideration is whether such fluctuations in $C(K_E, K_Z)$ (or ZKE) might represent an observational artifact due to the limited domain over which velocities could be measured. This could lead, for example, to artificial fluctuations in the apparent $C(K_E, K_Z)$ as individual Rossby wave trains passed through the field of view. Accordingly, we determined the typical drift period of observed wave trains across the field of view from a sample of space-time spectra of radial velocity fluctuations along lines of constant radius (from Fourier analysis of azimuth-time sections, such as illustrated in Fig. 6). The corresponding dominant period, τ_{drift} , was estimated for each experiment and is shown in Table II. In the event, τ_{drift} varied between 350 s and 1500 s, and there appeared to be only a weak correlation between τ_{drift} and either τ_{conv} or τ_{ZKE} , although a component identifiable as τ_{drift} was apparent in many of the spectra of EKE variations. Moreover, the numerical values of τ_{drift} were found to differ from the other time scales by quite large factors, from which we may conclude that wave drift effects within the observational window do not appear to be responsible for the apparent fluctuations in $C(K_E, K_Z)$.

More physical explanations for such fluctuations on the observed time scale τ_{conv} might include effects associated either with frictional damping or advection. The appropriate time scale for frictional damping is the Ekman spin down time scale, τ_E , while an estimate of the advective time scale can be obtained as

$$\tau_p \simeq \frac{L_R}{u_{rms}} \simeq \frac{1}{\sqrt{u_{rms}^E \beta_T}}. \quad (27)$$

Both of these time scales, τ_E and τ_p , were computed for each experiment and are listed in Tables I and II. Both time scales clearly correlate quite strongly with τ_{conv} , though τ_E differs from τ_{conv} by a factor ~ 2 –5. Linear fits between τ_{conv} and τ_E or τ_p lead to gradients of 4.8 ± 0.98 and 0.995 ± 0.19 , respectively, with correlation coefficients of 0.94 and 0.95. The corresponding fitted y -intercepts were -282 ± 234 s for τ_p , while the line against τ_E has y -intercept $-2.5 \pm 1.2 \times 10^3$ s. Such an analysis would seem to favor τ_p as consistent with the observed scaling of τ_{conv} , although τ_E is also highly correlated. But given the nonlinear origin of $C(K_E, K_Z)$, it is perhaps intuitively reasonable that the advective scale τ_p might represent the likely time scale of variations in eddy forcing of the zonal flow. It is notable, however, that τ_{conv} is not at all correlated with that of the fluctuations in ZKE itself, the time scale of which does not seem to scale with any obvious parameter.

VI. KE SPECTRA

The kinetic energy spectra provide another important set of diagnostics that can provide valuable insights into the distribution and exchange of energy between different scales.

The natural decomposition of velocity and other fields within the cylindrical domain is via a Fourier-Bessel transform in azimuth and radius, respectively. However, the use of Bessel functions in the radial direction is complicated by the existence of an inner cylindrical boundary in the present experiment. This makes it inconvenient to utilize combinations of J_n and Y_n Bessel functions in the Bessel decomposition in the radial direction. Through the use of the coordinate transformation described in Section II (see Eqs. (2) and (3)), the flow patterns were placed into a pseudo-Cartesian domain, with axes aligned parallel to the azimuthal and radial directions, scaled by the mean radius r_0 . So, it was much more convenient to carry out the analysis assuming Cartesian geometry, though it was then necessary to take some account of the systematic radial variation in the amplitudes of fluctuations, due in part to the cylindrical geometry. The eddy fields were extended in the x -direction to match the extent in y by repeating data columns from the same field.

From an inspection of the radial dependence of the variance of non-axisymmetric eddy velocities in the time mean across all experiments, it was found that, except near the innermost radii, the eddy variance followed a variation close to r^{-3} . Accordingly, in order to be able to use fast Fourier methods in both the azimuthal *and* radial directions, the velocity field was scaled by a “pre-whitening” factor of $(r/r_0)^{3/2}$ before computing the 2D fast Fourier transform. This resulted in relatively clean spectra for further analysis and interpretation.

Zonostrophic flow is commonly characterized by differing structures in kinetic energy spectra between the zonal and non-zonal flow components.^{26,29,32} For the non-zonal spectrum, a Kolmogorov-Batchelor-Kraichnan inertial range is anticipated for scales larger than the forcing scale k_ξ (cf. Section III A) over the range $k_\xi \gg |k| \gtrsim k_\beta$ of the form

$$E_R(k) = C_K \epsilon^{2/3} k^{-5/3} \quad (28)$$

(where C_K is a universal constant ~ 5 – 6) within which energy is transferred upscale. In contrast, the zonal mean spectrum is anticipated to be independent of ϵ and to be solely governed by stability bounds on its vorticity structure in equilibrium between upscale forcing and dissipation at large scales. In fully zonostrophic flows, the spectrum is expected to take the universal, self-similar form

$$E_Z(k) = C_Z \beta^2 k^{-5}, \quad (29)$$

where C_Z is another universal constant ≈ 0.5 , e.g., Refs. 26, 29, and 32. This may be contrasted with the “modal” spectrum in the KBK range of the form

$$E_Z^m(k) = C_K \epsilon^{2/3} k^{-8/3}, \quad (30)$$

which would be expected in a relatively isotropic flow.²¹

To explore the relevance of these forms of spectra in the present experiments, we follow the work of Galperin *et al.*^{26,29,32} and partition the 2D KE spectra into a zonal mean part $E_Z(|k|)$ and a residual spectrum $E_R(|k|)$ such that the total kinetic energy E_T is given by

$$E_T = \int E_Z(K) + E_R(K) dK \quad (31)$$

where K is the total wavenumber ($K = [k_x^2 + k_y^2]^{1/2}$). The zonal mean spectrum at positive and negative k_y was summed to obtain the KE as a function of (positive-definite) total wavenumber K . The derivation of E_R entails integrating the 2D non-zonal spectrum $E_E(k_x, k_y)$ in θ to obtain

$$E_R(K) dK = \left(\int E_E(k_x, k_y) K d\theta \right) dK. \quad (32)$$

These 1D spectra were then obtained for each of the five main experiments in the present study to obtain spectra of E_Z and E_R , shown as “compensated” spectra in Figure 12, by dividing E_T and E_R by Eq. (28) and E_Z by Eqs. (29) and (30), respectively.

All five of the experiments shown indicate a range of wave numbers over which the total and residual spectra, $E_T(K)$ and $E_R(K)$, follow quite closely the KBK form in both spectral slope and amplitude. This KBK range varies significantly between runs, however, with all experiments departing from this idealized form for $K \gtrsim 20$ rad m⁻¹. In most cases, this leads to a steeper slope, perhaps indicating the role of viscous diffusion and bottom friction in damping the eddy flow at small scales.

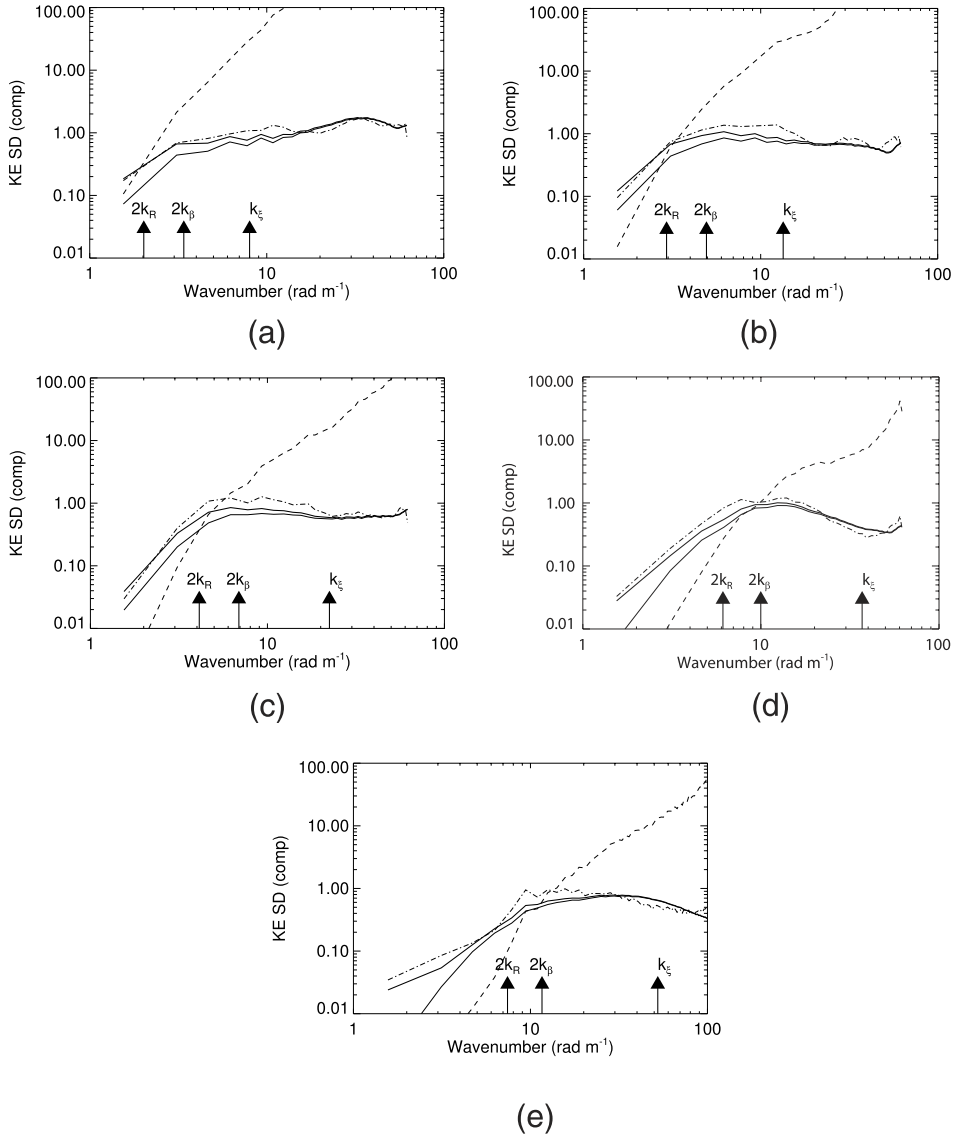


FIG. 12. Time-averaged, compensated kinetic energy spectra for various values of rotation period and water depth. Parameters correspond to (a) $\tau_R = 320$ s, $D = 0.8$ m ($\beta^* = 43$), (b) $\tau_R = 160$ s, $D = 0.8$ m ($\beta^* = 91$), (c) $\tau_R = 80$ s, $D = 0.8$ m ($\beta^* = 180$), (d) $\tau_R = 40$ s, $D = 0.8$ m ($\beta^* = 395$), and (e) $\tau_R = 40$ s, $D = 0.45$ m ($\beta^* = 581$). Thick solid lines represent the total kinetic energy spectrum, averaged over all orientations, while thinner solid lines show the spectrum with the zonal mean component removed, both compensated by dividing by the KBK spectrum assuming the values of ϵ in Table II. The dashed lines show the zonal mean spectrum, normalized by the zonostrophic zonal mean spectrum given by Eq. (29), while the dashed-dotted lines show the zonal mean spectrum normalized by the “modal” spectra given by Eq. (30). The nominal values of $2k_R$, $2k_\beta$, and k_ϵ are indicated by the arrows.

At the larger scales, however, the total and residual spectra reach a maximum at a wavenumber that increases as Ω was increased, with the widest $k^{-5/3}$ range occurring at the lowest value of Ω . For the lowest rotation case (Fig. 12(a)), there is even some evidence of the spectrum rising to a secondary peak around $K \sim 30\text{--}35$ rad m $^{-1}$, corresponding to a wavelength of around 18-20 cm. This may be close to the energy injection scale, representing the scale at which the eddy forcing is imposed.

The plateaux in E_R shown in Fig. 12 indicate a resultant amplitude around unity in each case, though the precise amplitude of each plateau varies somewhat between experiments. This would seem to suggest that the assumed value of ϵ in Eq. (28) may not be quite consistent with the “true” value of the upscale cascade rate. Accordingly, if we assume the flat segment of the compensated

E_R spectra should correspond to an amplitude of unity, we can estimate a corrected value of ϵ consistent with Eq. (28) and the resulting values are listed as ϵ_{spec} in Table II. These values show a remarkable consistency across the set of experiments, with all experiments with a mean depth of 0.8 m exhibiting a value for $\epsilon_{spec} \sim 5 \times 10^{-10} \text{ W kg}^{-1}$ and the shallower experiment (with mean depth of 0.45 m) producing a value nearly twice the size. This would appear to be consistent with the increased horizontal energy density for the latter run, since the heating rate was the same in all cases.

At the largest scales, the total energy spectrum becomes dominated by the zonal mean flow, whose spectra are much steeper than the residual spectra, though somewhat less steep than the anticipated K^{-5} of the fully zonostrophic regime. The actual E_Z spectra seem closer to a K^{-4} dependence, perhaps consistent with the expectation that these flows are only marginally zonostrophic and unable to fully develop the steep, zonostrophic spectrum in their zonal flow structure (cf. questions (v) and (vi) in Section I). In this case, the zonal spectra seem to conform more closely to the “modal” $K^{-8/3}$ form, certainly for $K \gtrsim k_\beta$, with only a marginal tendency to steepen in the range $2k_R < K < 2k_\beta$.

VII. DISCUSSION

In these experiments, we have sought to extend the range and duration of the earlier series of convectively driven rotating flows on a topographic beta-plane,^{53,54} but using thermal forcing instead of salt-driven convection. The former clearly has a number of advantages over the latter in being more straightforward to apply in a controlled way uniformly across the experimental domain and in enabling the forcing to be maintained almost indefinitely. The results presented here, with a similar applied buoyancy flux, though with opposite topographic slope, are qualitatively and quantitatively similar in many respects to the cases studied in our salt-driven experiments which included a topographically imposed vorticity gradient. Convective vortices were seen to evolve into larger structures through vortex mergers and other nonlinear interactions, eventually forming a more or less barotropic equilibrated flow in which zonal jets emerged spontaneously as a result of direct wave-zonal flow interactions, interspersed with an apparently chaotic pattern of waves and vortices. In each case, the whole pattern appeared to equilibrate after only a few hours (corresponding to a few Ekman spin down time scales), after which there were few discernible changes in either flow structure or amplitude. The resulting flows were characterized by kinetic energy spectra that exhibited a $K^{-5/3}$ range in the residual E_R spectrum and a steeper slope (though less steep than -5) in the zonal E_Z spectrum (cf. question (vi) in Section I).

In the new experiments presented here, however, we have explored a much wider range of rotation rates and related parameters, such as Rhines length scales and deformation radii, in order to examine how various flow properties scale with Ω and β_T and several other parameters. The use of an oppositely sloping lower boundary to our earlier experiments has enabled us to show that the basic flow regimes are not greatly sensitive to the sense of background vorticity gradient due to the topography other than to reverse the sense of phase propagation of Rossby-like waves. Zonal jets were still found to arise principally through the action of direct eddy-zonal flow interactions, much as anticipated in a number of modeling studies based on a quasi-linear approach.^{30,31,33} The presence of a $K^{-5/3}$ range in the residual E_R spectrum, however, and the apparent growth and merging of convective structures, suggests that a conventional quasi-isotropic turbulent upscale cascade is also present in these flows (cf. question (iii) in Section I), and it would be of interest to examine this in more detail in further diagnostic studies.

A novel and unexpected result of the present work was the finding that the zonal kinetic energy production rate, $C(K_E, K_Z)$, is very strongly variable in time (by around an order of magnitude; cf. question (iv) in Section I), though such large time variations do not seem to be strongly reflected in corresponding fluctuations in ZKE. The time scale of variations in $C(K_E, K_Z)$ was apparently consistent with the inertial time scale $\tau_p = 1/\sqrt{(u_{rms}^E \beta_T)}$, which one might associate with variations related to vorticity advection, though could also be consistent with a time scale related to Ekman damping. The large difference in the time scale τ_E to that of $C(K_E, K_Z)$ itself, however,

would seem to make this less plausible as the principal mechanism determining such variations in $C(K_E, K_Z)$. Such strong variability in time, if found to be a general trait of near-zonostrophic flows, could have important implications for interpreting measurements of eddy-zonal flow interactions in geophysical systems, such as in the atmospheres of gas giant planets and in the Earth's oceans.

The jet formation process observed in our experiments is also evidently not much affected by the relatively small values of L_D^{int} , despite the fact that values of β_D^{*int} and $\tilde{\beta}^{int}$ in Table II and Section IV A would suggest otherwise.^{23,41,42} But this refers only to the baroclinic flow components that do not participate in the main jet-forming process (cf. questions (i) and (vii) in Section I), the latter of which appears to be mainly barotropic. This has important implications for the interpretation of the corresponding processes active in the oceans and in the atmospheres of gas giant planets and in assessing when barotropic simplified models are valid to simulate the main dynamical interactions.^{22,23,28} The external deformation radius in the oceans is of order 2000 km compared with around 50–100 km for the internal deformation radius, indicating the possibility that “zonation” in the oceans may be similarly unaffected by baroclinic effects up to scales comparable with L_D^{ext} . Estimates of L_D in the atmospheres of Jupiter and Saturn range from ~ 750 km to ~ 4000 km at 30° latitude,^{23,73} leading to a value for $\tilde{\beta}$ in the range 1.5–30 or so, based on recent estimates⁵ of $\epsilon \sim 0.5\text{--}1 \times 10^{-5} \text{ m}^2 \text{ s}^{-3}$. The larger values of L_D and $\tilde{\beta}$, however, correspond to gravity wave speeds measured following the comet Shoemaker-Levy 9 impact, which probably represent values appropriate to the strongly stratified upper stratosphere, whereas the lower values represent the (much less strongly stratified) troposphere. The cloud-level flow on Jupiter, however, is clearly highly anisotropic and zonal, indicating that the tropospheric estimate of $\tilde{\beta}$ has a similar status to the value of $\tilde{\beta}^{int}$ in our experiments, namely, that the jet-like anisotropic flow is predominantly barotropic.

A key new result has shown that the lateral scale of the zonal jets obtained seems to scale closely with either a Rhines scale L_R or the Vallis-Maltrud scale L_β (cf. questions (i) and (ii) in Section I). Although this was not unexpected, since it features clearly in a number of previous experimental and modeling studies,^{23,28,34,52,55} the measured variation was surprisingly clear. The measurements were not sufficiently accurate or sensitive, however, to distinguish whether the dominant scaling parameter was a Rhines scale based on either the rms eddy velocity, the zonal or total horizontal velocities, or L_β . The lack of distinction between L_R and L_β arose because the experiments were only able to explore a very narrow range of zonostrophy parameter, R_β , which defines the ratio of L_R to L_β .

This narrow accessible range of R_β is not unduly surprising, given its very weak dependence on parameters under an experimentalist's control. Given the definition of R_β in Eq. (16), this leads to

$$R_\beta \sim [\epsilon \beta^2 \tau_E^5]^{1/20}, \quad (33)$$

indicating that R_β depends most strongly on the Ekman time scale τ_E and least strongly on ϵ itself. For four out of the five experiments reported here, ϵ was approximately constant at around $7\text{--}8 \times 10^{-10} \text{ m}^2 \text{ s}^{-3}$ (see Table II). The remaining parameters, β and τ_E , depend on Ω such that $R_\beta \sim \Omega^{-1/40}$, leading to a relative range in R_β of just 5% over the full range of Ω covered, as shown in Table II. Even with such a small variation in R_β , however, a number of flow properties (e.g., ZKE/TKE or ZKE/EKE, α_I , and $C(KE, KZ)/\epsilon$) were seen to change systematically over the range covered (cf. questions (i)–(iii) in Section I).

An alternative approach was suggested from the experiments of Aubert *et al.*,⁵² who found that the ratio of zonal to radial velocity amplitudes in their experiments on convection in a rotating, spherical cavity scaled approximately as

$$\frac{\bar{u}_\theta}{\bar{u}_r} \sim \text{Re}_\ell^{2/3} E^{1/6}, \quad (34)$$

where $\text{Re}_\ell = (\text{Ra}_Q/P^2)^{3/5} E^{4/5}$ is the local convective Reynolds number, Ra_Q is the flux Rayleigh number, P the Prandtl number, and E the Ekman number. In our case, given a fixed heating rate (and Ra_Q) and P for most of our experiments, this would suggest a dependence of \bar{u}_θ/\bar{u}_r on E as $E^{7/10}$, which at least indicates a trend somewhat consistent with our results in Table II. But the trend in \bar{u}_θ/\bar{u}_r with E is not monotonic for our data, unlike the correlation with R_β , and it was not clear from

the subsequent work, e.g., of Gillet *et al.*⁵⁵ that the relationship in Eq. (34) was universal, whereas the correlation with R_β shown here seems much clearer.

The quite strong changes with R_β in our experiments may suggest that these flows are very close to the threshold of the fully zonostrophic regime, since numerical model studies^{26,29,32,34} suggest that flow properties (such as eddy diffusivities⁷⁴) change rapidly with R_β around a transitional value of $R_\beta \approx 1.5$. It is possible, therefore, that a modest increase in R_β , e.g., by increasing the boundary slope and/or depth of the system, might be sufficient to produce much more strongly zonal flows characteristic of that regime. Achieving substantial increases in R_β in these types of experiments towards values typical of gas giant planet atmospheres⁵ or even idealized numerical models,^{23,34} however, presents a major challenge to experimenters.

ACKNOWLEDGMENTS

The authors are grateful to Boris Galperin, Stefania Espa, and Semion Sukoriansky for discussions that were helpful in the interpretation of our experimental results, and to G. K. Vallis and an anonymous referee for their constructive comments on an earlier version of this manuscript. We are grateful to the HYDRALAB program, funded by the EC Contract *Access to Major Research Infrastructures*, for their support during the experimental design and acquisition phase of this project. P.L.R., P.H.T.R., R.M.B.Y., and H.Y. acknowledge additional support from the UK Science and Technology Facilities Council, and T.N.L.J., R.D.W., R.M.B.Y., and K.M.-Y. from the UK Natural Environment Research Council. P.L.R. is grateful to the Kavli Institute for Theoretical Physics at the University of California, Santa Barbara for its hospitality during the writing of this paper, for which partial support by the National Science Foundation under Grant No. PHY11-25915 is acknowledged. Under this program, this paper has Preprint No. NSF-KITP-14-065.

- ¹ J. P. Peixoto and A. H. Oort, *Physics of Climate* (American Institute of Physics, New York, 1992).
- ² T. Schneider, "The general circulation of the atmosphere," *Annu. Rev. Earth Planet. Sci.* **34**, 655–688 (2006).
- ³ A. Ingersoll, T. Dowling, P. Gierasch, G. Orton, P. Read, A. Sánchez-Lavega, A. Showman, A. Simon-Miller, and A. Vasavada, "Dynamics of Jupiter's atmosphere," in *Jupiter: The Planet, Satellites and Magnetosphere*, edited by F. Bagenal, T. E. Dowling, and W. B. McKinnon (Cambridge University Press, 2004), pp. 105–128.
- ⁴ A. R. Vasavada and A. Showman, "Jovian atmospheric dynamics: An update after Galileo and Cassini," *Rep. Prog. Phys.* **68**, 1935–1996 (2005).
- ⁵ B. Galperin, R. Young, S. Sukoriansky, N. Dikovskaya, P. Read, A. Lancaster, and D. Armstrong, "Cassini observations reveal a regime of zonostrophic macroturbulence on Jupiter," *Icarus* **229**, 295–320 (2014).
- ⁶ C. Porco, R. West, A. McEwen, A. Del Genio, P. Ingersoll, A. P. Thomas, S. Squyres, L. Dones, C. Murray, T. Johnson, J. Burns, A. Brahic, G. Neukum, J. Veverka, J. Barbara, T. Denk, M. Evans, J. Ferrier, P. Geissler, P. Helfenstein, T. Roatsch, H. Throop, M. Tiscareno, and A. Vasavada, "Cassini imaging of Jupiter's atmosphere, satellites, and rings," *Science* **299**, 1541–1547 (2003).
- ⁷ K. J. Richards, N. A. Maximenko, F. O. Bryan, and H. Sasaki, "Zonal jets in the Pacific Ocean," *Geophys. Res. Lett.* **33**, L03605, doi:10.1029/2005gl024645 (2006).
- ⁸ H.-P. Huang, A. Kaplan, E. N. Curchitser, and N. M. Maximenko, "The degree of anisotropy for mid-ocean currents from satellite observations and an eddy-permitting model simulation," *J. Geophys. Res.* **112**, C09005, doi:10.1029/2007jc004105 (2007).
- ⁹ I. Kamenkovich, P. Berloff, and J. Pedlosky, "Role of eddy forcing in the dynamics of multiple zonal jets in a model of the North Atlantic," *J. Phys. Oceanogr.* **39**(6), 1361–1379 (2009).
- ¹⁰ T. Nadiga and D. N. Straub, "Alternating zonal jets and energy fluxes in barotropic wind-driven gyres," *Ocean Modell.* **33**, 257–269 (2010).
- ¹¹ N. A. Maximenko, B. Bang, and H. Sasaki, "Observational evidence of alternating zonal jets in the world ocean," *Geophys. Res. Lett.* **32**, L12607, doi:10.1029/2005GL022728 (2005).
- ¹² N. A. Maximenko, O. V. Melnichenko, P. P. Niiler, and H. Sasaki, "Stationary mesoscale jet-like features in the ocean," *Geophys. Res. Lett.* **35**, L08603, doi:10.1029/2008gl033267 (2008).
- ¹³ L. M. Ivanov, C. A. Collins, and T. M. Margolina, "System of quasi-zonal jets off California revealed from satellite altimetry," *Geophys. Res. Lett.* **36**, L03609, doi:10.1029/2008gl036327 (2009).
- ¹⁴ M. Schlax and D. Chelton, "The influence of mesoscale eddies on the detection of quasi-zonal jets in the ocean," *Geophys. Res. Lett.* **35**, L24602, doi:10.1029/2008GL035998 (2008).
- ¹⁵ D. Olbers, D. Borowski, C. Völker, and J.-O. Wölff, "The dynamical balance, transport and circulation of the Antarctic Circumpolar Current," *Antarctic Sci.* **16**, 439–470 (2004).
- ¹⁶ A. Isobe, "Driving mechanism of band structure of mean current over the continental shelf," *J. Phys. Oceanogr.* **34**, 1839–1855 (2004).
- ¹⁷ P. H. Diamond, S.-I. Itoh, K. Itoh, and T. S. Hahm, "Zonal flows in plasma—A review," *Plasma Phys. Controlled Fusion* **47**, R35–R161 (2005).
- ¹⁸ P. B. Rhines, "Waves and turbulence on a β -plane," *J. Fluid Mech.* **69**, 417–443 (1975).

- ¹⁹ P. B. Rhines, "Jets," *Chaos* **4**, 313–339 (1994).
- ²⁰ H.-P. Huang, B. Galperin, and S. Sukoriansky, "Anisotropic spectra in two-dimensional turbulence on the surface of a rotating sphere," *Phys. Fluids* **13**, 225–240 (2001).
- ²¹ S. Sukoriansky, B. Galperin, and N. Dikovskaya, "Universal spectrum of two-dimensional turbulence on a rotating sphere and some basic features of atmospheric circulation on giant planets," *Phys. Rev. Lett.* **89**(12), 124501 (2002).
- ²² J. Aubert, S. Jung, and H. L. Swinney, "Observations of zonal flow created by potential vorticity mixing in a rotating fluid," *Geophys. Res. Lett.* **29**, 1876, doi:10.1029/2002GL015422 (2002).
- ²³ K. S. Smith, "A local model for planetary atmospheres forced by small-scale convection," *J. Atmos. Sci.* **61**, 1420–1433 (2004).
- ²⁴ S. Danilov and D. Gurarie, "Scaling, spectra and zonal jets in beta-plane turbulence," *Phys. Fluids* **16**, 2592–2603 (2004).
- ²⁵ M. Rempel, "Solar differential rotation and meridional flow: The role of a subadiabatic tachocline for the Taylor–Proudman balance," *Astrophys. J.* **622**, 1320–1332 (2005).
- ²⁶ B. Galperin, S. Sukoriansky, N. Dikovskaya, P. L. Read, Y. H. Yamazaki, and R. Wordsworth, "Anisotropic turbulence and zonal jets in rotating flows with a β -effect," *Nonlinear Proc. Geophys.* **13**, 83–98 (2006).
- ²⁷ J. Aurnou, M. Heimpel, and J. Wicht, "The effects of vigorous mixing in a convective model of zonal flow on the ice giants," *Icarus* **190**, 110–126 (2007).
- ²⁸ R. K. Scott and L. M. Polvani, "Forced-dissipative shallow-water turbulence on the sphere and the atmospheric circulation of the giant planets," *J. Atmos. Sci.* **64**, 3158–3176 (2007).
- ²⁹ S. Sukoriansky, N. Dikovskaya, and B. Galperin, "On the arrest of inverse energy cascade and the Rhines scale," *J. Atmos. Sci.* **64**, 3312–3327 (2007).
- ³⁰ P. A. O'Gorman and T. Schneider, "Recovery of atmospheric flow statistics in a general circulation model without nonlinear eddy–eddy interactions," *Geophys. Res. Lett.* **34**, L22801, doi:10.1029/2007GL031779 (2007).
- ³¹ R. D. Wordsworth, "A phase-space study of jet formation in planetary-scale fluids," *Phys. Fluids* **21**, 056602 (2009).
- ³² B. Galperin, S. Sukoriansky, and N. Dikovskaya, "Geophysical flows with anisotropic turbulence and dispersive waves: Flows with a β -effect," *Ocean Dyn.* **60**, 427–441 (2010).
- ³³ K. Srinivasan and W. R. Young, "Zonostrophic instability," *J. Atmos. Sci.* **69**, 1633–1656 (2012).
- ³⁴ R. K. Scott and D. G. Dritschel, "The structure of zonal jets in geostrophic turbulence," *J. Fluid Mech.* **711**, 576–598 (2012).
- ³⁵ T. Gastine, J. Wicht, and J. M. Aurnou, "Zonal flow regimes in rotating anelastic spherical shells: An application to giant planets," *Icarus* **225**, 156–172 (2013).
- ³⁶ T. Gastine, M. Heimpel, and J. Wicht, "Zonal flow regimes in rotating anelastic spherical shells: An application to giant planets," *Phys. Earth Planet. Inter.* **232**, 36–50 (2014).
- ³⁷ R. H. Kraichnan, "Inertial ranges in two-dimensional turbulence," *Phys. Fluids* **10**, 1417–1423 (1967).
- ³⁸ R. H. Kraichnan, "Inertial range transfer in two- and three-dimensional turbulence," *J. Fluid Mech.* **47**, 525–535 (1971).
- ³⁹ J. G. Charney, "Geostrophic turbulence," *J. Atmos. Sci.* **28**, 1087–1095 (1971).
- ⁴⁰ R. Salmon, "Baroclinic instability and geostrophic turbulence," *Geophys. Astrophys. Fluid Dyn.* **15**, 167–211 (1980).
- ⁴¹ A. Okuno and A. Masuda, "Effect of horizontal divergence on the geostrophic turbulence on a beta-plane: Suppression of the Rhines effect," *Phys. Fluids* **15**, 56–65 (2003).
- ⁴² I. Saito and K. Ishioka, "Angular distribution of energy spectrum in two-dimensional β -plane turbulence in the long-wave limit," *Phys. Fluids* **25**, 076602 (2013).
- ⁴³ J. A. Whitehead, "Mean flow generated by circulation on a β -plane: An analogy with the moving flame experiment," *Tellus* **27**, 358–364 (1975).
- ⁴⁴ A. C. de Verdiere, "Quasi-geostrophic turbulence in a rotating homogeneous fluid," *Geophys. Astrophys. Fluid Dyn.* **15**, 213–251 (1980).
- ⁴⁵ J. Sommeria, S. D. Meyers, and H. L. Swinney, "Laboratory model of a planetary eastward jet," *Nature* **337**, 58–61 (1989).
- ⁴⁶ J. Sommeria, S. D. Meyers, and H. L. Swinney, "Experiments on vortices and rossby waves in eastward and westward jets," in *Nonlinear Topics in Ocean Physics*, edited by A. R. Osborne (North Holland, Amsterdam, 1991), pp. 227–269.
- ⁴⁷ S. A. Condie and P. B. Rhines, "A convective model for the zonal jets in the atmospheres of Jupiter and Saturn," *Nature* **367**, 711–713 (1994).
- ⁴⁸ J.-B. Manneville and P. Olson, "Banded convection in rotating fluid spheres and the circulation of the Jovian atmosphere," *Icarus* **250**, 242–250 (1996).
- ⁴⁹ P. J. Mason, "Baroclinic waves in a container with sloping endwalls," *Philos. Trans. R. Soc., A* **278**, 397–445 (1975).
- ⁵⁰ M. E. Bastin and P. L. Read, "Experiments on the structure of baroclinic waves and zonal jets in an internally heated rotating cylinder of fluid," *Phys. Fluids* **10**, 374–389 (1998).
- ⁵¹ R. D. Wordsworth, P. L. Read, and Y. H. Yamazaki, "Turbulence, waves and jets in a differentially heated rotating annulus experiment," *Phys. Fluids* **20**, 126602 (2008).
- ⁵² J. Aubert, D. Brito, H.-C. Nataf, P. Cardin, and J.-P. Masson, "A systematic experimental study of rapidly rotating spherical convection in water and liquid gallium," *Phys. Earth Planet. Inter.* **128**, 51–74 (2001).
- ⁵³ P. L. Read, Y. H. Yamazaki, S. R. Lewis, P. D. Williams, K. Miki-Yamazaki, J. Sommeria, H. Didelle, and A. Fincham, "Jupiter's and Saturn's convectively-driven banded jets in the laboratory," *Geophys. Res. Lett.* **31**, L22701, doi:10.1029/2004GL020106 (2004).
- ⁵⁴ P. L. Read, Y. H. Yamazaki, S. R. Lewis, P. D. Williams, R. D. Wordsworth, K. Miki-Yamazaki, J. Sommeria, H. Didelle, and A. Fincham, "Dynamics of convectively driven banded jets in the laboratory," *J. Atmos. Sci.* **64**, 4031–4052 (2007).
- ⁵⁵ N. Gillet, D. Brito, D. Jault, and H.-C. Nataf, "Experimental and numerical studies of convection in a rapidly rotating spherical shell," *J. Fluid Mech.* **580**, 83–121 (2007).
- ⁵⁶ S. Espa, G. Di Nitto, and A. Cenedese, "The emergence of zonal jets in forced rotating shallow water turbulence: A laboratory study," *Europhys. Lett.* **92**, 34006 (2010).
- ⁵⁷ G. Di Nitto, S. Espa, and A. Cenedese, "Simulating zonation in geophysical flows by laboratory experiments," *Phys. Fluids* **25**, 086602 (2013).

- ⁵⁸ A. G. Slavin and Y. D. Afanasyev, "Multiple zonal jets on the polar beta plane," *Phys. Fluids* **24**, 016603 (2012).
- ⁵⁹ Y. Zhang and Y. D. Afanasyev, "Beta-plane turbulence: Experiments with altimetry," *Phys. Fluids* **26**, 026602 (2014).
- ⁶⁰ C. A. Smith, K. G. Speer, and R. W. Griffiths, "Multiple zonal jets in a differentially heated rotating annulus," *J. Phys. Oceanogr.* **44**, 2273–2291 (2014).
- ⁶¹ J. Paret and P. Tabeling, "Experimental observation of the two-dimensional inverse energy cascade," *Phys. Rev. Lett.* **79**, 4162–4165 (1997).
- ⁶² A. M. Fincham and G. R. Spedding, "Low cost, high resolution DPIV for measurement of turbulent fluid flow," *Exp. Fluids* **23**, 449–462 (1997).
- ⁶³ A. M. Fincham and G. Delerce, "Advanced optimization of correlation imaging velocimetry algorithms," *Exp. Fluids* **29**(1), S013–S022 (2000).
- ⁶⁴ H. J. S. Fernando, R.-R. Chen, and D. L. Boyer, "Effects of rotation on convective turbulence," *J. Fluid Mech. Digital Arch.* **228**, 513–547 (1991).
- ⁶⁵ T. Maxworthy and S. Narimousa, "Unsteady, turbulent convection into a homogeneous, rotating fluid, with oceanographic applications," *J. Phys. Oceanogr.* **24**, 865–887 (1994).
- ⁶⁶ J. Marshall and F. Schott, "Open-ocean convection: Observations, theory and models," *Rev. Geophys.* **37**, 1–64, doi:10.1029/98RG02739 (1999).
- ⁶⁷ Y. Nakagawa and P. Frenzen, "A theoretical and experimental study of cellular convection in rotating fluids," *Tellus* **7**, 1–21 (1955).
- ⁶⁸ See supplementary material at <http://dx.doi.org/10.1063/1.4928697> for movies showing the evolution of velocity and potential vorticity fields and wave-like propagation of vortices and jet meanders.
- ⁶⁹ P. Rhines, "The dynamics of unsteady currents," in *The Sea* (Wiley, 1977), Vol. 6, pp. 189–318; available at <http://www.hup.harvard.edu/catalog.php?isbn=9780674017351>.
- ⁷⁰ G. K. Vallis, *Atmospheric and Oceanic Fluid Dynamics* (Cambridge University Press, Cambridge, UK, 2006).
- ⁷¹ M. E. Maltrud and G. K. Vallis, "Energy spectra and coherent structures in forced two-dimensional and beta-plane turbulence," *J. Fluid Mech. Digital Arch.* **228**, 321–342 (1991).
- ⁷² G. K. Vallis and M. E. Maltrud, "Generation of mean flows and jets on a beta plane and over topography," *J. Phys. Oceanogr.* **23**, 1346–1362 (1993).
- ⁷³ R. K. Achterberg and A. P. Ingersoll, "A normal-mode approach to Jovian atmospheric dynamics," *J. Atmos. Sci.* **46**, 2448–2462 (1989).
- ⁷⁴ S. Sukoriansky, B. Galperin, and N. Dikovskaya, "Transport of momentum and scalar in turbulent flows with anisotropic dispersive waves," *Geophys. Res. Lett.* **36**, L14609, doi:10.1029/2009GL038632 (2009).